




Statistical properties of surface gravity waves and freak wave occurrence in crossing sea states

S. Liu ^{1,2} T. Waseda,³ J. Yao ^{1,2} and X. Zhang ^{1,2,*}

¹*State Key Laboratory of Ocean Engineering, School of Naval Architecture, Ocean and Civil Engineering, Shanghai Jiao Tong University, Shanghai 200240, China*

²*Collaborative Innovation Center for Advanced Ship and Deep-Sea Exploration (CISSE), Shanghai 200240, China*

³*Graduate School of Frontier Sciences, University of Tokyo, Kashiwa, Chiba 277-8563, Japan*



(Received 21 February 2022; accepted 9 June 2022; published 20 July 2022)

A series of direct numerical simulations of the Euler equation are conducted using a high-order spectral (HOS) method to investigate the nonlinear statistics and freak wave occurrences in crossing sea states. Several crossing sea states with varying frequency spectra, directional spreading, and crossing angles between two wave components are chosen for the computations. The dynamical statistics of surface waves are reported, including the wave spectra, the exceedance probability of wave crest amplitude, the probability density distribution of surface elevation, the kurtosis and skewness, the freak wave occurrence probability, and the freak wave shape. A Benjamin-Feir index, named as CBFI, is derived to measure the third-order nonlinearity effects for crossing seas. This parameter allows us to forecast the probability of freak waves, and it is validated by a series of HOS simulations. Furthermore, the freak wave shape is more notably influenced by changes to the crossing angle rather than each component's frequency or directional spectral bandwidth. Increasing the crossing angle reduces the vertical and horizontal asymmetries in the mean propagation direction.

DOI: [10.1103/PhysRevFluids.7.074805](https://doi.org/10.1103/PhysRevFluids.7.074805)

I. INTRODUCTION

A freak wave (also called a rogue wave or extreme wave) is an anomalous, short-term wave that is much higher than expected for the sea state. There are many reasons for the formation of freak waves, such as the refraction due to bathymetry or currents, modulational instability, and directional and dispersive focusing [1–4]. As one of the most possible mechanisms for the formation of freak waves, modulational instability is a physical phenomenon in which a plane wave is unstable under sideband perturbations (see the general overview in Ref. [5]). For the past 20 years, the effects of modulational instability on the statistical properties of gravity waves and freak wave formation in unimodal-spectra sea states have been studied theoretically, experimentally, and numerically. Modulational instability plays a significant role in the occurrence of freak waves in sea states featuring narrow-banded spectra in both the frequency and directional domains [6]. However, under an increase in directional spreading, the importance of modulational instability is reduced [7–10]. In addition, the shallow water depth can suppress these effects of modulational instability [11,12]. Because the modulational instability appears to be present only in narrow-banded spectra and sufficiently deep water, increasing concerns have been raised about whether modulational instability still remains in realistic sea conditions (e.g., Ref. [13]).

*xinshuz@sjtu.edu.cn

Although most of the previous studies have focused on sea states characterized by single-peaked spectra, a significant percentage of sea states that are more complex than single-peaked spectral ones [14]. Wave systems characterized by two spectral peaks with different propagation directions (also known as crossing sea states) are considered to be a situation in which the effects of modulational instability may be enhanced. The nonlinear interaction between two wave systems appears to be a cause of freak wave occurrences. There is much evidence that unusual and extreme wave phenomena occur in crossing seas. The famous Draupner wave was found to be generated when swell waves propagate to the wind sea, according to the hindcast data from the European Centre for Medium-Range Weather Forecasts by Adcock *et al.* [15]. Fedele *et al.* [13] successfully recreated the Draupner wave and another two typical freak waves (the Andrea and Killard waves) in numerical simulations. They found that the formation of those waves mainly results from the second-order bound nonlinearities instead of the modulational instability. Mcallister *et al.* [16] successfully recreated the Draupner wave in a circular wave basin and found that a crossing angle between 60° and 120° is needed to reproduce the waveform. Ferreira *et al.* [17] studied freak waves in the Campos basin, off the coast of Brazil. They only observed freak waves in sea states assumed to be those of crossing seas. Rosenthal [18] also found evidence that freak waves occur in crossing sea states. In addition, numerous ship accidents have been reported in crossing sea conditions [19], particularly when two wave systems have similar wave periods and noncollinear wave directions [20]. Typical ship accidents that have occurred in crossing seas include the Suwa Maru accident [21], the Louis Majesty accident [22], and the Prestige accident [23]. Fedele *et al.* [24] studied the El Faro accident based on the third-order generation model and high-order spectral (HOS) method. Their results showed the probability that the El Faro encounters a rogue wave while the drifting is relatively large, around $1/400$ over a time interval of 10 minutes. A complete understanding of the modulational instability in crossing sea states can help us to better understand the freak wave phenomenon and to avoid ship accidents.

Modulational instability has been investigated within the framework of nonlinear Schrödinger (NLS) equations for crossing seas consisting of two identical long-crested wave systems. Onorato *et al.* [25] studied the modulational instability of two wave systems with the same frequency but different propagation directions, using the coupled nonlinear Schrödinger (CNLS) equations derived from the Zakharov equation. Their results suggested that the existence of another wave system can result in an increase of the instability growth rates and the expansion of the instability region, and more freak waves can be expected in crossing sea states with crossing angles less than approximately 70° . An extension of the obtained results in Onorato *et al.* [25] to the more general cases of two-dimensional perturbations was performed by Shukla *et al.* [26]. Onorato *et al.* [27] presented a further detailed derivation of the CNLS equations and a discussion of the coefficients in front of the dispersive and nonlinear terms with the support of numerical simulations. The results showed that crossing angles between 20° and 60° are the most likely to increase modulational instability and establish a freak wave sea. These theoretical results based on the CNLS equations were validated in Toffoli *et al.* [28], where both laboratory experiments and numerical simulations were performed to study the effect of the crossing angle on the kurtosis, which can quantitatively describe the third-order nonlinearity. The effects of the frequency spectrum and directional spreading were not considered.

To include the effect of directional spreading in crossing seas, Bitner-Gregersen and Toffoli [29] conducted numerical simulations of crossing directional seas based on hindcast data. Their results showed that the maximum kurtosis occurred at a crossing angle of about 40° . A more recent experimental study on crossing directional seas was reported in Luxmoore *et al.* [30]; there, the results showed that the third-order nonlinearity is more affected by the directional spreading of each wave components, rather than the crossing angles between the two wave components.

Regarding crossing seas with separated peak frequencies, Gramstad and Trulsen [31] derived a coupled version of the broadband modified NLS equations introduced by Trulsen and Dysthe [32], and they studied the modulational instability of two interacting uniform wave trains. However, the results derived from the NLS equations may suffer from nonphysical extensions of the instability

regions beyond the bandwidth constraints of the equations. More recently, Gramstad *et al.* [33] derived the nonlinear evolution equation for two crossing waves in the framework of Zakharov equation, which is valid for arbitrary-bandwidth perturbations. Based on this equation, they considered both the case that two wave systems have the same peak frequency and the case that two wave systems are very well separated in frequency. The values of maximum kurtosis were used to assess the modulational instability in crossing waves. The effects of crossing angle, differences in terms of dominant wave frequency and energy between the two wave systems, and spectral shape on the modulational instability were investigated via numerical simulations. Their results showed that maximum kurtosis is expected for relatively large or small crossing angles, with a minimum of around 90° ; furthermore, the expected maximum crest height is almost independent of the crossing angle. Brennan *et al.* [34] investigated the emergence of freak wave in crossing seas based on the HOS method. Two classes of crossing sea states were considered: one using the spectra of the Draupner wave crossing at different angles (“Draupner-Draupner”) and the other using a Draupner’s spectrum crossed with a narrow-banded JONSWAP spectrum of a smaller peak frequency (“Draupner-JONSWAP”). The effects of crossing angle on the evolution of kurtosis and skewness were investigated. However, they only studied the crossing systems consisting of two short-crested waves with crossing angle $\Delta\theta = 22.5^\circ, 40^\circ, \text{ and } 90^\circ$.

The Benjamin-Feir index (BFI) is usually adopted to predict the importance of modulational instability throughout the wave spectrum in a field. Janssen [6] introduced (for the first time) the BFI in terms of the ratio between wave steepness and spectral bandwidth. Subsequently, further extensions to include directional spreading (i.e., the two-dimensional Benjamin-Feir index, BFI_{2D}) have been made (e.g., Refs. [8,10,35]). To date, the BFI or BFI_{2D} has been considered a good indicator for estimating the third-order nonlinearity effect. However, most of the applications are focused on unimodal waves. More recently, by using an empirical relationship based on the BFI_{2D} proposed by Mori *et al.* [35], it is found that the kurtosis can be estimated well from the directional spreading [30]. However, that study only considered the crossing seas consisting of directional waves with relatively small crossing angles (below 40°). This motivated us to assess the performance of the BFI from Mori *et al.* [35] under a wider range of crossing waves and to develop a robust approach for estimating the modulational instability in a crossing wave field.

With the increase in modulational instability, the occurrence probability of freak waves increases; meanwhile, the shape of the freak wave varies significantly. Because previous studies primarily focused on the probability of freak wave occurrence, increasing concerns have been raised over the past few years regarding the effect of modulational instability on freak wave shapes. Fujimoto *et al.* [36] investigated the impact of the four-wave quasisresonance on freak wave shapes, using the HOS model based on the observed and simulated directional spectra. Modulational instability is a special case of four-wave quasisresonance. It was revealed that the kinematics of the freak wave groups seem to be better indicators for the significance of the four-wave interaction, compared to the occurrence probability. Xie *et al.* [37] performed numerical simulations of four-wave resonance between two gravity waves and found that strong resonant interactions can lead to the bending and subsequent splitting of crests and troughs. However, the features of the freak wave shape under crossing-wave conditions are rarely mentioned. Furthermore, the effects of the crossing angle and spectral shape on the freak wave shape remain unclear.

In the present study, we systematically investigated the effects of the frequency spectrum and directional spreading of individual wave components, as well as the crossing angle on the wave statistical properties and freak waves. We fully characterized the wave statistics, including the wave spectra evolution, the probability density distribution of surface elevation, the exceedance probability distributions of wave crests, kurtosis, and skewness. Unlike previous studies, which mainly focused on the occurrence probability of freak waves, the freak wave shape is extensively studied here. In addition, we derived a modified BFI for crossing seas; this is a valid spectral parameter for quantification of the effect of modulational instability on wave statistical properties and freak wave occurrence probability.

The remainder of this paper is organized as follows. Section II presents the set-up for the HOS simulations and initial conditions of the simulated crossing seas. In Sec. III, the validation of the numerical simulations is demonstrated by comparison with the experiments. The results and discussions for the statistical properties of waves including the evolution of wave spectrum, skewness, kurtosis, the probability density function of the surface elevations, and the exceedance probability of wave crests are presented and discussed in Sec. III. Section IV shows the probability of freak wave occurrence and the derivation of a coupled BFI (CBFI) for crossing seas. Section V investigates the freak wave shapes. Finally, our conclusions are provided in Sec. VI.

II. SET-UP FOR NUMERICAL SIMULATIONS

Numerical simulations of nonlinear crossing wave fields were performed using the HOS method [38,39], which directly solves the field equations with the kinematic and dynamic boundary conditions on the free surface, expressed in the Zakharov's form [40]:

$$\eta_t = -\nabla\eta \cdot \nabla\phi^s + (1 + |\nabla\eta|^2) \cdot \phi_z \quad \text{at } z = \eta(\mathbf{x}, t), \quad (1)$$

$$\phi_t^s + g\eta = -\frac{1}{2} \cdot |\nabla\phi^s|^2 + \frac{1}{2}(1 + |\nabla\eta|^2)\phi_z^2 \quad \text{at } z = \eta(\mathbf{x}, t), \quad (2)$$

where $\phi^s(\mathbf{x}, t) = \phi(\mathbf{x}, \eta(\mathbf{x}, t), t)$ is defined as the surface velocity potential, η is the free-surface elevation, $\mathbf{x} = (x, y)$, and $\nabla = (\partial/\partial x, \partial/\partial y)$. The HOS method has been widely used to simulate the evolution of surface gravity waves (e.g., Refs. [9,10,28,29,33,41,42]).

The computational domain is a square of $32\lambda_p \times 32\lambda_p$ with periodic boundary conditions, where λ_p is the peak wavelength. A small domain size in numerical simulations may lead to underestimation of the statistics, e.g., kurtosis [33]. Kokina and Dias [43] have carefully tested the influence of the size of the computational domain on the HOS simulation of Draupner wave. They suggested that statistical properties should be computed over an area of at least 4 km^2 . Considering that the mean wavelength of Draupner wave is around 200 m, the suggested computational domain size is around $10\lambda_p \times 10\lambda_p$. Therefore, the domain size of $32\lambda_p \times 32\lambda_p$ adopted in the present study is sufficient to generate convergent results. 1024×1024 nodes are selected to capture the free-surface elevation and velocity potential (i.e., about 32 points per dominant wavelength). The nonlinear order $M = 3$ is adopted to consider the three-wave and four-wave nonlinear interactions [44]. A fourth-order Runge-Kutta time integration with $\Delta t = T_p/50$ is used (T_p is the period corresponding to the dominant wavelength λ_p), which meets the condition for the nonlinear problem $\Delta t^2 \leq 8/k_m$ (k_m corresponds to the maximum wave number, see Dommermuth and Yue [38]). The total computation duration of the HOS simulations is set as $t = 100T_p$. The obtained surface elevation and velocity potential are measured at five-wave intervals (i.e., at $t = 5, 10, \dots, 95, 100T_p$). The higher-order nonlinearity usually leads to a deviation from normality within a few peak periods [6]. The evolution duration considered in this study is sufficient to capture the formation of extreme waves. The obtained free-surface elevations are then used to calculate the statistical properties of the wave field. To achieve results of statistical significance, 30 repetitions with different random phases are performed for a given spectrum. By increasing the number of random realizations, we expected to minimize the effects related to the size of the computational domains [45]. We verified that the above-mentioned number of realizations can reliably estimate the statistical properties (see Appendix for details).

An energy dissipation model suggested by Xiao *et al.* [10] is adopted to treat the energy dissipation induced by wave breaking. The parameters of the filter are set to $\beta_1 = 8$ and $\beta_2 = 30$, which means the components with wave number $k > 8k_p$ are filtered out. Kokina and Dias [43] discussed the influence of these parameters by comparing the performance of a strong filter with $\beta_1 = 8$ and $\beta_2 = 30$ and a weak filter with $\beta_1 = 30$ and $\beta_2 = 10$. They found that the patterns of the evolution of the kurtosis and skewness in these filters are almost the same. But, with the use of the weak filter, the kurtosis and skewness increase more quickly and their average values are higher due to the reduced energy loss. The strong filter has been verified to correlate well with the

laboratory measurements of unimodal irregular waves (see Xiao *et al.* [10]). Here, to compare with the experiments of bimodal waves, we also used the strong filter.

The initial velocity potential used for the HOS model was obtained from the initial surface elevation based on the linear wave theory. To ensure a stable simulation, the nonlinear terms in the free-surface boundary conditions are ramped up smoothly over a short time $\sim 3T_p$ [46]. The influence of the ramping period is examined and discussed in Appendix.

Herein, the initial wave field is composed of two identical irregular waves propagating in different directions. Each of the irregular wave systems is described by the Joint North Sea Wave Project (JONSWAP) spectrum with a cosine-squared directional distribution. Random phases are assigned to the initial spectrum. The JONSWAP spectrum is defined as

$$F(\omega) = \frac{\alpha g^2}{\omega^5} \exp\left[-\frac{5}{4}\left(\frac{\omega}{\omega_p}\right)^{-4}\right] \gamma \exp\left[-\frac{(\omega-\omega_p)^2}{(2\sigma^2\omega_p^2)}\right], \quad (3)$$

where ω is the wave frequency, ω_p the peak wave frequency, α the Phillips parameter, and γ the peak enhancement factor specifying the frequency spectral bandwidth; σ has the standard values: 0.07 for $\omega < \omega_p$ and 0.09 for $\omega \geq \omega_p$. The energy spreading in the directional domain is given by a cosine-squared function [10],

$$D(\theta) = \begin{cases} \frac{2}{\Theta} \cos^2\left(\frac{\pi\theta}{\Theta}\right) & \text{for } |\theta| \leq \Theta/2 \\ 0 & \text{for } |\theta| > \Theta/2 \end{cases} \quad (4)$$

where Θ is the directional spreading width (also called the spreading angle) and θ is the wave propagation direction. For each wave system, the directional wave spectrum is obtained using $S(\omega, \theta) = F(\omega) \cdot D(\theta)$.

We described each wave component with a fixed significant wave height $H_s = 0.06$ m and dominant wave period $T_p = 1$ s. This configuration corresponds to a wave steepness of $k_p H_s / 4 = 0.06$, where k_p is the dominant wave number corresponding to the dominant wavelength. The following crossing angles between the two wave systems are considered: $\Delta\theta = 20^\circ, 40^\circ, 60^\circ$, and 80° . The wave propagation directions for each wave system are set as symmetrical to maximize the uniformity in the numerical wave basin. To consider the directional spreading effect, different values of the spreading angle Θ are adopted, ranging from fairly long-crested (small Θ) to fairly short-crested (large Θ) waves. The following values are chosen: $\Theta = 5^\circ, 15^\circ$, and 30° . To consider the effect of the spectral bandwidth, different values of the peak enhancement factor γ are used, ranging from fairly narrow-banded (large γ) to fairly broad-banded (small γ) waves. The following values are selected: $\gamma = 2, 5$, and 8 . The corresponding directional distribution and frequency spectra are shown in Fig. 1.

The selected test conditions are listed in Table I. The key parameters are the crossing angle between the two wave components $\Delta\theta$, the peak enhancement factor γ , and directional spreading width Θ . In set A, the effect of the crossing angle on the modulational instability, and statistical properties are tested by varying $\Delta\theta$ between 20° and 80° . Here the sea states consist of two nearly long-crested waves. In set B, the effect of $\Delta\theta$ in crossing short-crested sea states is tested. In set C, the effect of frequency spectral bandwidth is tested by varying γ between 2 and 8. Finally, in set D, we study the effect of directional spreading by changing Θ .

III. MODEL VALIDATION

Before discussing the results, the wave statistical properties in HOS simulations are compared with those from the experiments to test the reliability of the present numerical model. Two classes of experiments are selected: one consists of two nearly long-crested waves by Toffoli *et al.* [28], Sabatino and Serio [47], the other is crossing directional seas by Luxmoore *et al.* [30]. It should be noted that the wave conditions in Sabatino and Serio [47] are the same as the crossing seas studied

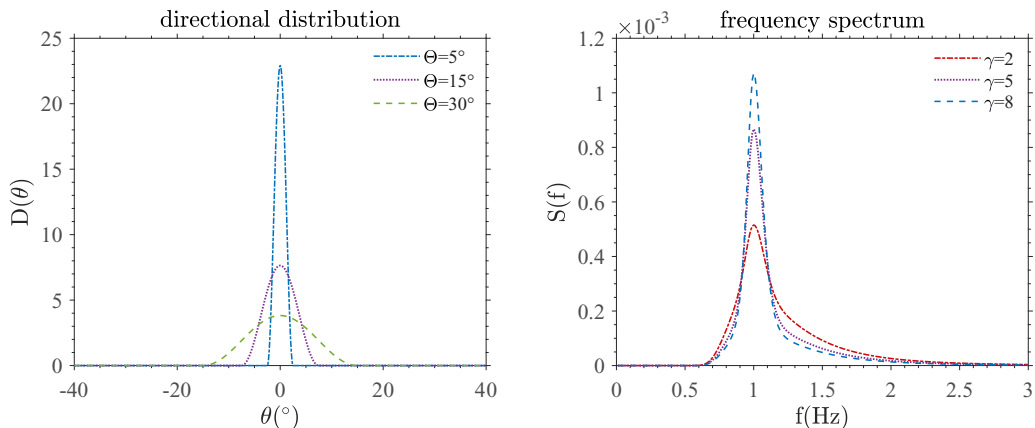


FIG. 1. The directional distribution and frequency spectra of the initial crossing sea state.

by Toffoli *et al.* [28]. The significant wave height of a single peak in Toffoli *et al.* [28] is 0.068 m and around 0.058 m in Luxmoore *et al.* [30]. The peak wave period in both of them is fixed at 1 s.

Figure 2 compares the kurtosis and skewness. The left panel corresponds to the results for the crossing long-crested waves compared with those in Toffoli *et al.* [28] and Sabatino and Serio [47], and the right panel corresponds to the results for the crossing short-crested waves compared with Luxmoore *et al.* [30]. The comparisons show that, in both long-crested and short-crested cases, the HOS data are in good agreement with the experiments. These tests demonstrate the reliability and accuracy of the present HOS model for crossing wave simulations.

Figure 3 compares the variation of the zeroth-order moment of wave spectrum between HOS simulations and experimental observations. The left and right panels show the nearly long-crested cases and short-crested cases, respectively. It is found that the present HOS simulations obtained satisfactory agreement over the reported range of crossing angles.

To examine the numerical results, the exceedance probability distribution of the wave crests is compared with the experimental results reported by Sabatino and Serio [47]. Two examples recorded at different times are shown in Fig. 4. Note that the experimental data used here are recorded at two different positions $x/\lambda_p = 9.5$ and 22.3. The corresponding times should be $t/T_p = 19.0$ and 44.6

TABLE I. Selected crossing wave tests.

	Test No.	H_s (m)	T_p (s)	$\Delta\theta$ ($^\circ$)	γ	Θ ($^\circ$)
Set A	01	0.06	1	20	5	5
	02	0.06	1	40	5	5
	03	0.06	1	60	5	5
	04	0.06	1	80	5	5
Set B	05	0.06	1	40	5	30
	06	0.06	1	60	5	30
	07	0.06	1	80	5	30
Set C	08	0.06	1	40	2	5
	02	0.06	1	40	5	5
	09	0.06	1	40	8	5
Set D	02	0.06	1	40	5	5
	10	0.06	1	40	5	15
	05	0.06	1	40	5	30

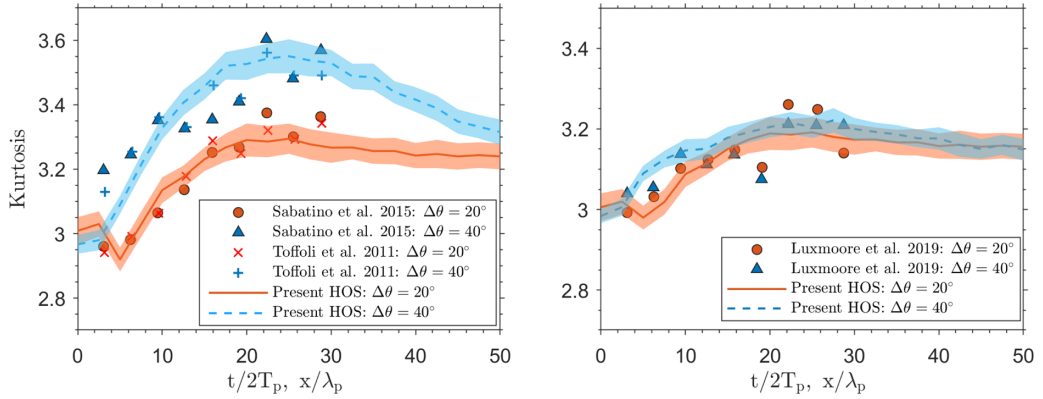


FIG. 2. Comparisons of the kurtosis and skewness between HOS results and experiments. $H_s = 0.068$ m and $T_p = 1$ s in Toffoli *et al.* [28] and Sabatino and Serio [47]. $H_s = 0.058$ m and $T_p = 1$ s in Luxmoore *et al.* [30].

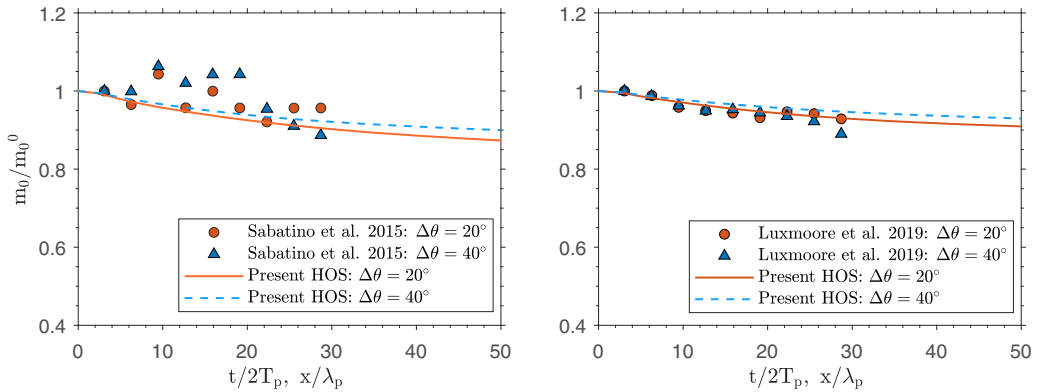


FIG. 3. Comparisons of the zeroth-order moment wave spectrum m_0 between HOS simulations and experimental observations. m_0^0 is the initial value. $H_s = 0.068$ m and $T_p = 1$ s in Toffoli *et al.* [28] and Sabatino and Serio [47]. $H_s = 0.058$ m and $T_p = 1$ s in Luxmoore *et al.* [30].

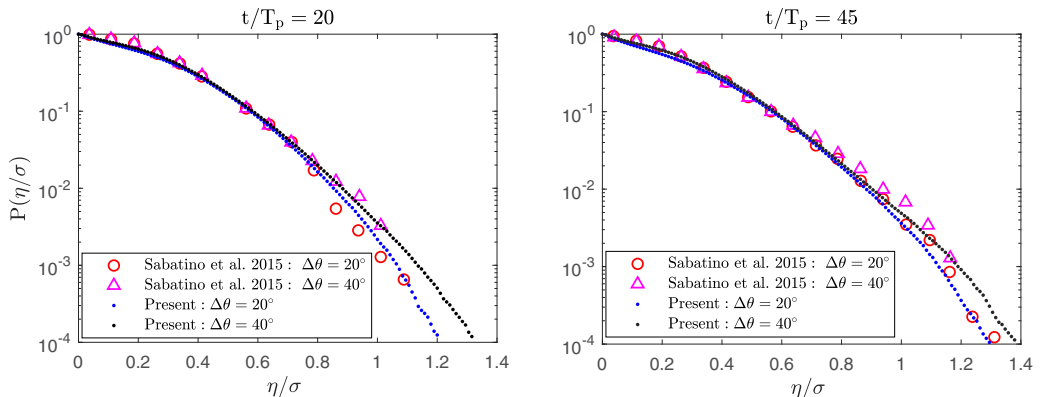


FIG. 4. Exceedance probability of the wave crest compared with previous experimental results [47] at different times.

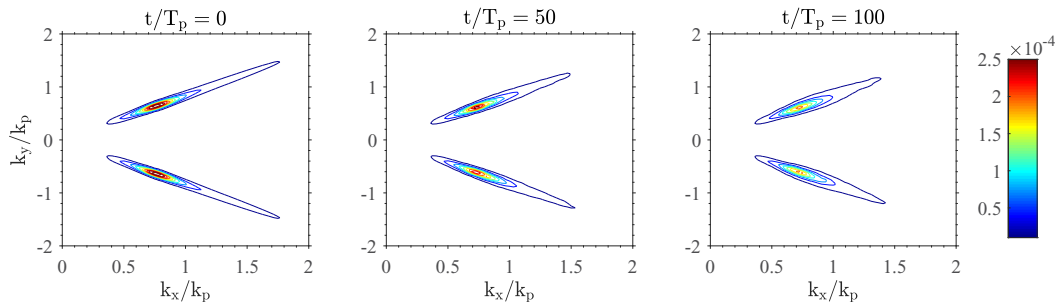


FIG. 5. Evolution of wave spectrum in crossing seas with $\Delta\theta = 80^\circ$, $\gamma = 5$, and $\Theta = 5^\circ$.

according to the relationship between the spatial and temporal variations determined by the group velocity. Considering the slowly varying wave crest distribution, we select $t/T_p = 20$ and 45 . As shown in the comparison, our numerical results are consistent with the experimental observations.

IV. SPECTRAL EVOLUTION AND NONLINEAR WAVE STATISTICS

A. Wave spectrum evolution

Herein we discuss the temporal evolution of the wave number spectra. Two examples for directional spectra at different nondimensional times $t/T_p = 0, 50$, and 100 are presented in Figs. 5 and 6. The spectra are obtained based on ensemble averaging over all realizations using a standard fast Fourier transform algorithm. When the waves propagate, the tail level of the wave number spectra decreases. This can be attributed to the use of an energy dissipation low-pass filter. The directional spreading is slightly broadened, especially in the long-crested case, as can be observed in Fig. 5.

Figure 7 presents the temporal variation of zeroth-order moment m_0 of the wave spectrum rescaled by its initial value m_0^0 . The significant wave height depends on the zeroth-order moment by $H_s = 4\sqrt{m_0}$. The left and right panels show the nearly long-crested $\Theta = 5^\circ$ cases (set A) and short-crested $\Theta = 30^\circ$ cases (set B), respectively. As shown, in set A or set B, m_0 decreases as the waves propagate, and it eventually reaches a quasisteady state. A similar trend was observed in the HOS simulation of unimodal seas [10]. Under an increasing crossing angle, the decreasing of m_0 becomes more significant. Comparing the left and right panels, the decrease of m_0 becomes more significant for smaller Θ .

B. Temporal evolution of kurtosis and skewness

Here we investigate the higher-order statistics, including the kurtosis λ_4 and skewness λ_3 . The former suggests an indication of the occurrence of extreme events, and the latter describes the

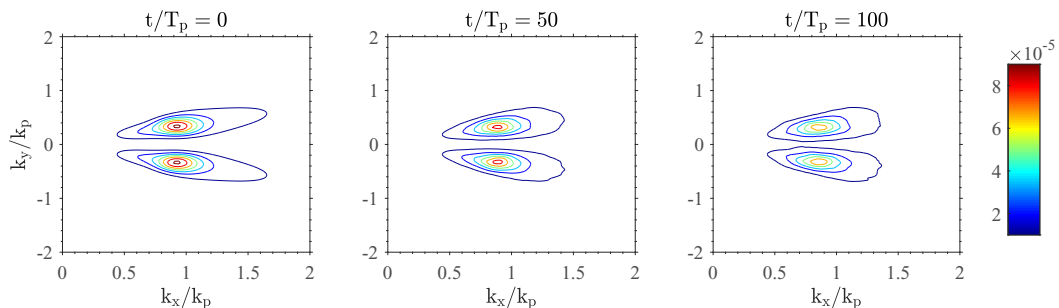


FIG. 6. Evolution of wave spectrum in crossing seas with $\Delta\theta = 40^\circ$, $\gamma = 5$, and $\Theta = 30^\circ$.

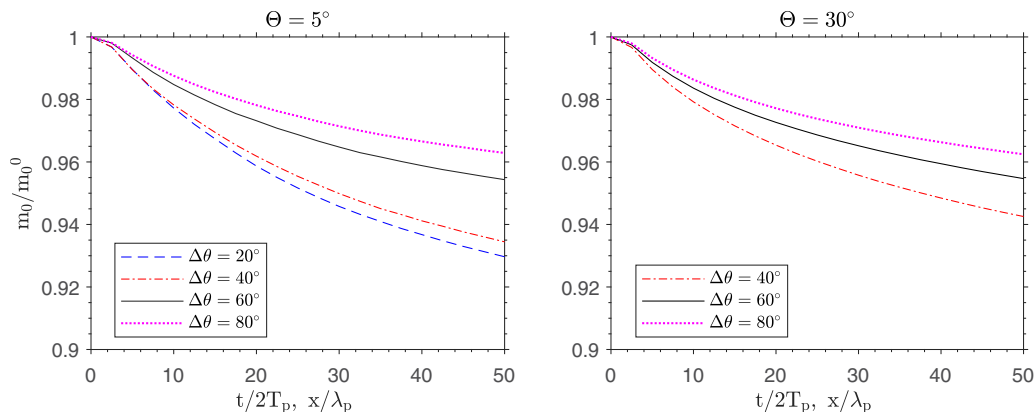


FIG. 7. Temporal variation of zeroth-order moment m_0 rescaled by the initial value m_0^0 . The left and right panels show the results for the nearly long-crested $\Theta = 5^\circ$ cases (set A) and short-crested $\Theta = 30^\circ$ cases (set B), respectively. The peak enhancement factor of the frequency spectrum is fixed at $\gamma = 5$.

vertical asymmetry of the wave profile. It should be noted that, in linear wave fields, the kurtosis and skewness are equal to 3 and 0, respectively [10,48].

The ensemble kurtosis and skewness, as a function of nondimensional time, are presented in Figs. 8 to 11. Huge datasets are needed to minimize the statistical uncertainty of these two statistics, especially the kurtosis. To quantify this, the 95% confidence bands are plotted, and these bands are calculated using the standard deviation over different random seeds. In all cases, the kurtosis increases from the Gaussian value of $\lambda_4 = 3$ over a timescale of around $50T_p$; then, it generally decreases to a quasistationary value. For the skewness, the growing stage is relatively short, $\sim 10T_p$. The observed tendencies of kurtosis and skewness are in reasonably good agreement with theoretical predictions by Fedele [49], as well as the experimental and numerical results [7,10,28]. Furthermore, we analyze the effects of the crossing angle, frequency spectral bandwidth, and directional spreading bandwidth on kurtosis in each figure, respectively.

Figure 8 illustrates the effect of the crossing angle between different wave systems, for long-crested ($\Theta = 5^\circ$) and moderate-banded ($\gamma = 5$) cases in set A. The kurtosis is smaller at crossing

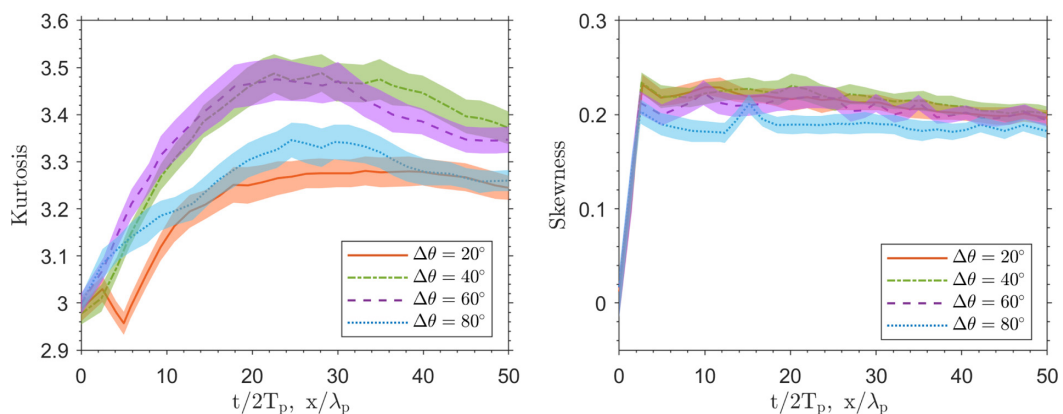


FIG. 8. Temporal evolution of kurtosis and skewness. The results show the effect of the crossing angle between different wave systems in nearly long-crested ($\Theta = 5^\circ$) and moderate-frequency bandwidth ($\gamma = 5$) seas. The shaded regions denote 95% confidence intervals.

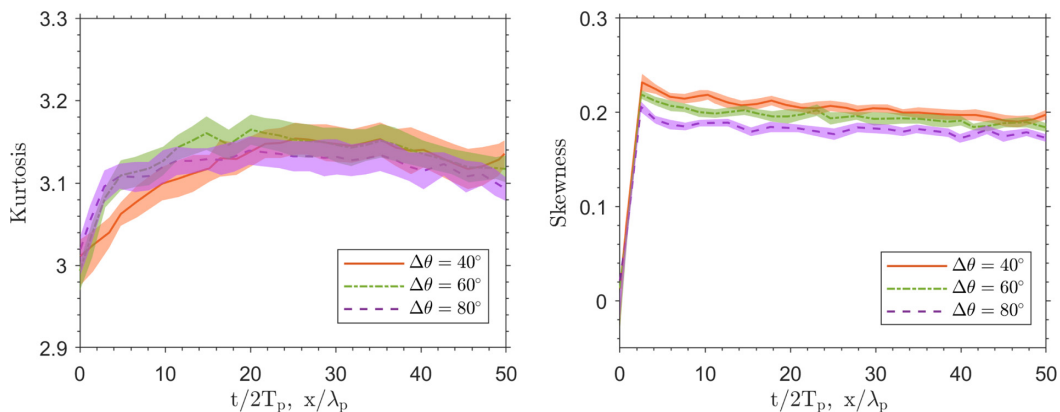


FIG. 9. Temporal evolution of kurtosis and skewness. The results show the effect of the crossing angle between different wave systems in nearly short-crested ($\Theta = 30^\circ$) and moderate-frequency bandwidth ($\gamma = 5$) seas. The shaded regions denote 95% confidence intervals.

angles $\Delta\theta = 20^\circ$ and 80° but are significantly increased for $\Delta\theta = 40^\circ$ and 60° . This observed dependency of the kurtosis on the crossing angle is consistent with the predictions derived from the coupled NLS equations by Onorato *et al.* [25] and Onorato *et al.* [27], where it was suggested that the maximum value was achieved for $40^\circ < \Delta\theta < 60^\circ$. According to the right panel of Fig. 8, the numerical results of skewness also agree with the experiments. Generally, waves with small crossing angles seem to possess larger skewness. The skewness is significantly smaller at $\Delta\theta = 80^\circ$, which indicates that the waves are more vertically symmetric in this case.

Figure 9 illustrates the effect of the crossing angle in nearly short-crested wave fields ($\Theta = 30^\circ$). Unlike the results of the long-crested cases (see Fig. 8), the increase in kurtosis for $40^\circ < \Delta\theta < 60^\circ$ seems to disappear for short-crested crossing systems. This is remarkably consistent with the results of previous studies [30,33]. In terms of skewness, when the crossing angle increases, the skewness value decreases.

Figure 10 shows the effect of the frequency bandwidths of the individual components on the ensemble kurtosis and skewness under a constant directional spreading $\Theta = 5^\circ$ and crossing angle $\Delta\theta = 40^\circ$. For a narrow-banded frequency spectrum of individual components, the effects of

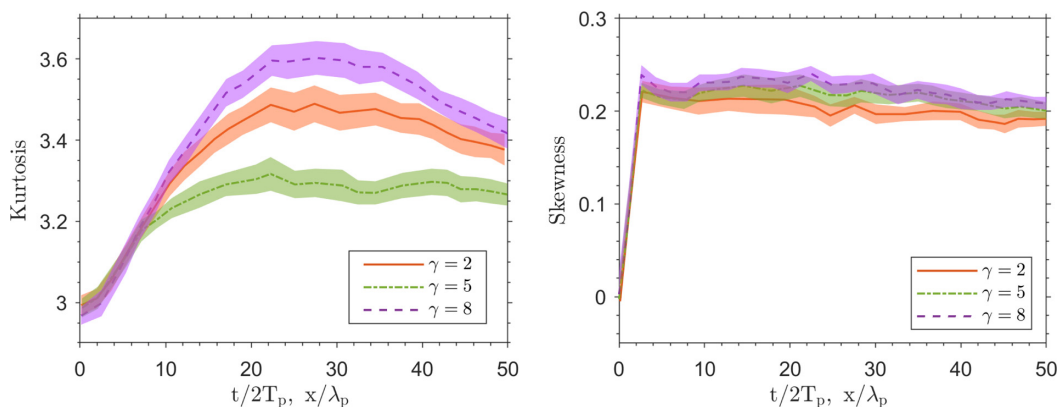


FIG. 10. Temporal evolution of kurtosis and skewness. The results show the effect of the frequency spectrum bandwidth but with a constant directional spreading bandwidth $\Theta = 5^\circ$ and crossing angle $\Delta\theta = 40^\circ$.

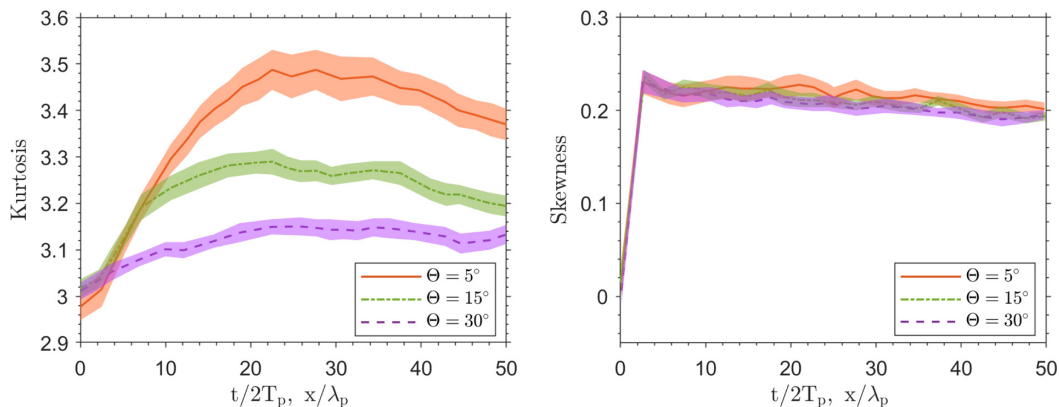


FIG. 11. Temporal evolution of kurtosis and skewness. The results show the effect of the directional spectrum bandwidth but under a constant frequency spectral bandwidth $\gamma = 5$ and crossing angle $\Delta\theta = 40^\circ$.

higher-order nonlinearity are more significant. Thus, it is not surprising to observe that both the kurtosis and skewness increase under a narrower frequency spectral bandwidth.

Figure 11 shows the effect of directional spreading of the individual components under a constant frequency bandwidth with $\gamma = 5$ and a crossing angle $\Delta\theta = 40^\circ$. We see that the kurtosis value decreases when the directional spreading angle Θ increases. This is because the effect of free-wave dynamics is usually less pronounced in a broad directional-spreading wave field [7,8]. Nevertheless, the value of skewness (which is less influenced by free-wave effects) is nearly independent of Θ , showing a slightly decreasing trend under an increase of Θ .

In addition, the evolution of kurtosis values in bimodal and unimodal seas are compared in Fig. 12. The initial conditions of the bimodal case are $\Delta\theta = 40^\circ$ and $\Theta = 5^\circ$. To examine the unimodal results of HOS, the experimental data of unimodal wave from Onorato *et al.* [7] are also plotted for reference. The initial condition of Onorato *et al.* [7] ($H_s = 0.06$ m, $T_p = 1$ s, $\gamma = 3$) is almost the same as that used in the present HOS ($H_s = 0.06$ m, $T_p = 1$ s, $\gamma = 5$). It is found that the kurtosis values in the bimodal and unimodal seas are very close, even though the wave steepness of the bimodal case is much larger than that of the unimodal case. This may be because the energy loss due to wave breaking in the bimodal case is more significant.

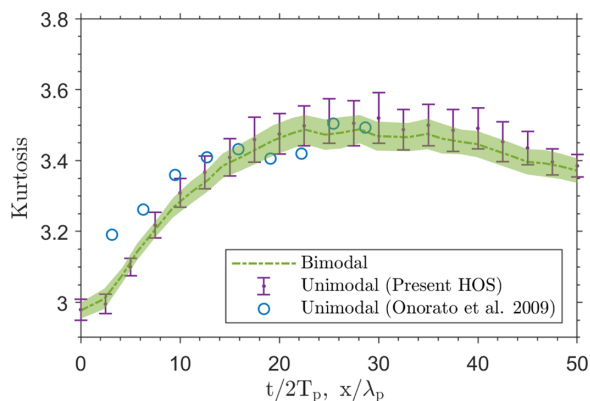


FIG. 12. The evolution of kurtosis in bimodal and unimodal seas. The experimental results of unimodal wave from Onorato *et al.* [7] are also presented for reference.

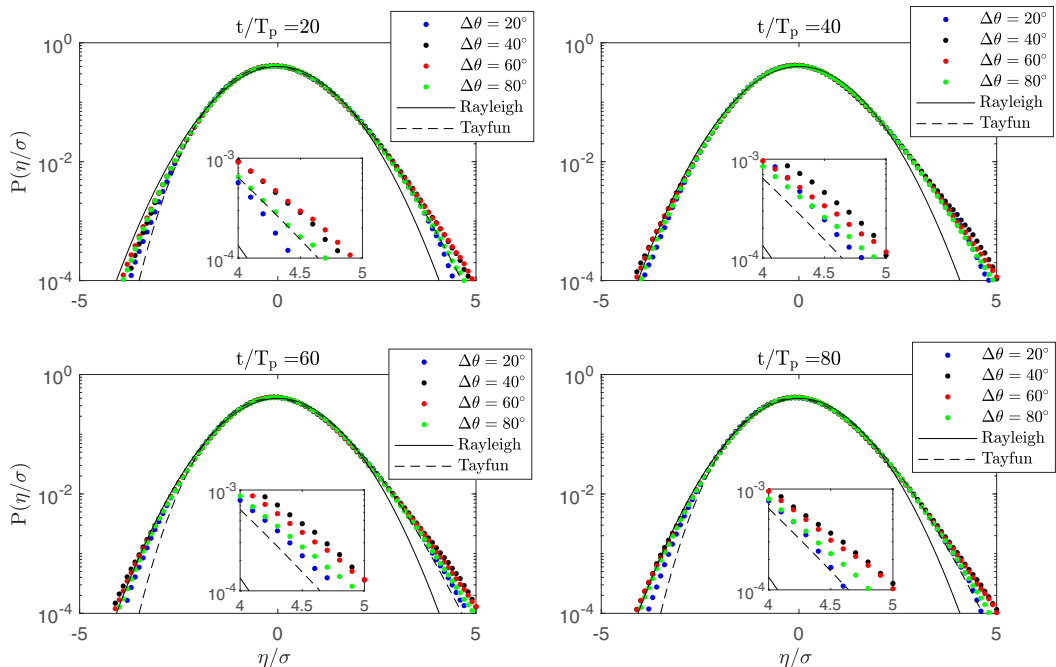


FIG. 13. Probability density function of the surface elevation at different times $t/T_p = 20, 40, 60,$ and 80 . The results show the effect of the crossing angle between different wave systems but under a constant directional spreading angle $\Theta = 5^\circ$ and frequency bandwidth $\gamma = 5$. The solid and dashed lines denote the Rayleigh and Tayfun distributions, respectively.

C. The probability density function of the surface elevation

In Figs. 13 to 16, we show the probability density function of the surface elevation at different times $t/T_p = 20, 40, 60,$ and 80 . For convenience, we scale the surface elevation using the standard deviation σ of the wave field at the concurrent time point. The numerical probability density functions are compared with the normal (Gaussian) and second-order distributions. The latter distribution was first derived by Tayfun [50]; an approximation of the expression can be found in Socquet-juglard *et al.* [51] and is expressed as

$$p(\eta) = \frac{1 - 7\sigma^2 k_p^2 / 8}{\sqrt{2\pi(1 + 3G + 2G^2)}} \exp\left(-\frac{G^2}{2\sigma^2 k_p^2}\right), \quad (5)$$

with

$$G = \sqrt{1 + 2k_p^2 \sigma \eta} - 1, \quad (6)$$

where σ is the standard deviation of the surface elevations.

The second-order effect produces higher crests and shallower troughs. As a result, the tails of the probability density function deviate from the normal distribution. Here both the second- and third-order nonlinearity effects are included in the present numerical simulation. As can be observed in Figs. 13 to 16, for all the tested cases, the upper tail is on or just above the Tayfun distribution (shown in the inset of the figures), and the lower tail is between the Rayleigh and Tayfun distributions. These results indicate that the crests are higher and the troughs are deeper than the second-order solutions. The discrepancy with the second-order model can be attributed to the effect of third-order nonlinearity.

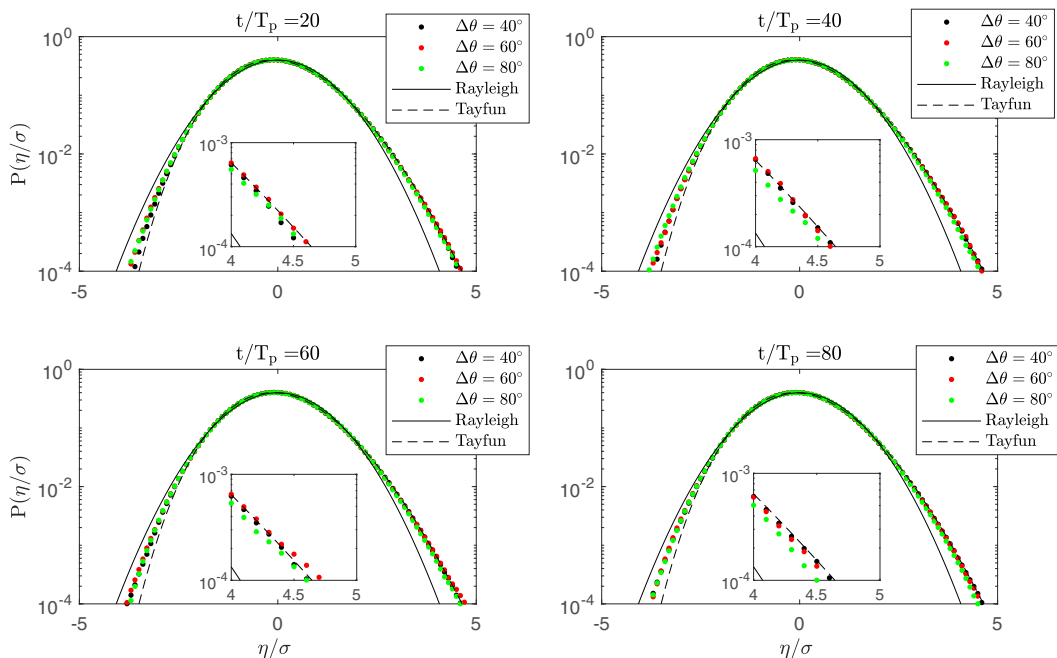


FIG. 14. Probability density function of the surface elevation at different times $t/T_p = 20, 40, 60,$ and 80 . The results show the effect of the crossing angle between different wave systems but with constant directional spreading $\Theta = 30^\circ$ and frequency bandwidth $\gamma = 5$. The solid and dashed lines denote the Rayleigh and Tayfun distributions, respectively.

The third-order effects can be measured quantitatively by the kurtosis value. Therefore, coinciding with the evolution of kurtosis, the lower and upper tail of the probability density function show a significantly increasing tendency during the initial stage $t/T_p = 20$ and 40 .

Furthermore, Fig. 13 shows that the crossing angle between the two wave components plays an important role in the probability density function of the surface elevation. The probability of higher and deeper wave elevations is more pronounced for the crossing seas with $\Delta\theta = 40^\circ$ and 60° , and they are less enhanced for $\Delta\theta = 20^\circ$ and 80° . The upper and lower tails of probability density distribution for $\Delta\theta = 40^\circ$ and 60° are closely grouped. These features correlate reasonably well with the kurtosis value. The cases with higher kurtosis show higher levels in the upper and lower tails.

In addition, Fig. 14 shows the effect of the crossing angle in nearly short-crested crossing seas. The influence of directional spreading of each wave component is included. As shown, the probability density distribution is nearly identical for different crossing angles. The upper tail is well described by the second-order Tayfun distribution, whereas the lower tail is above the Tayfun distribution. Again, the kurtosis is consistent with the feature of the probability density distribution—the kurtosis is closely grouped in the range from 3.1 to 3.2 (see Fig. 9) and the probability density distribution is nearly identical for the tests.

Figures 15 and 16 show the effects of the frequency spectral and directional spreading bandwidth, respectively. Under a narrower frequency spectrum or directional spreading, the probabilities of both higher and deeper wave elevations are increased. The kurtosis also correlates well with this feature (see Figs. 10 and 11).

D. Exceedance probability of wave crests

The traditional linear wave theory predicts Gaussian statistics for the wave surface. However, real waves are nonlinear, with the wave crests being sharper and the troughs being flatter. The

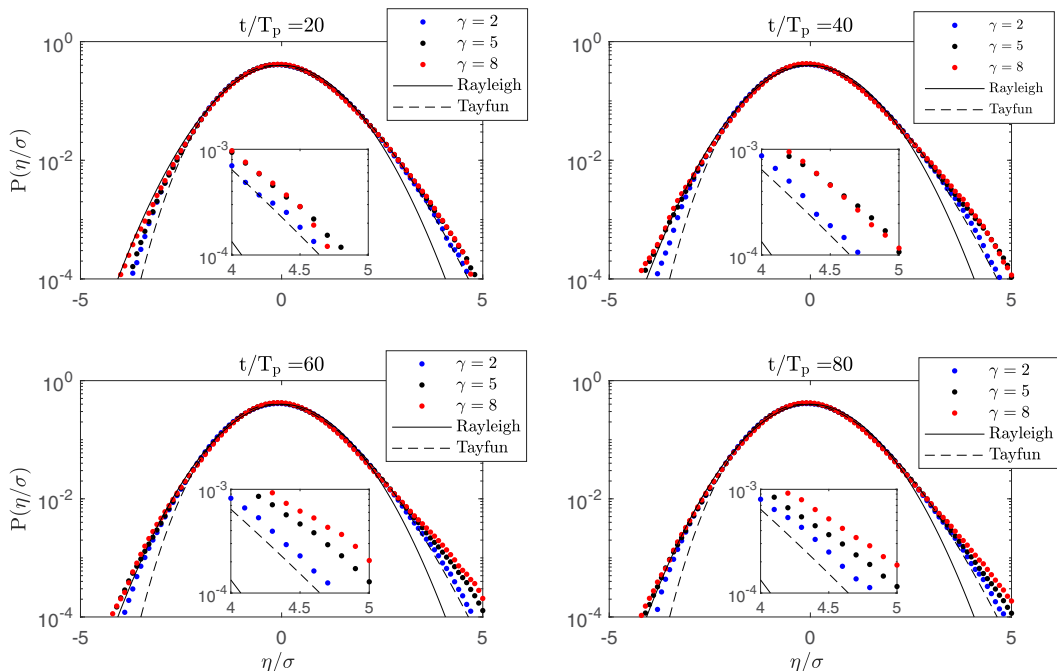


FIG. 15. Probability density function of the surface elevation at different times $t/T_p = 20, 40, 60,$ and 80 . The results show the effect of the frequency spectral bandwidth of individual components but with constant directional spreading $\Theta = 5^\circ$ and crossing angle $\Delta\theta = 40^\circ$. The solid and dashed lines denote the Rayleigh and Tayfun distributions, respectively.

Rayleigh distribution underestimates the probability of large crests. To overcome this problem, several semiempirical formulas have been proposed to describe the nonlinear wave crest distribution. Tayfun [50] has derived a second-order model for wave crest distribution. The exceedance probability is expressed as

$$p(\eta_c > \eta) = \exp \left[-\frac{8}{H_s^2 k_p^2} (\sqrt{1 + 2k_p \eta} - 1)^2 \right], \quad (7)$$

where η_c is the wave crest amplitude, which is defined as the local maximum of the wave surface.

In Figs. 17 and 18, the wave crest distributions at different times $t/T_p = 20, 40, 60,$ and 80 are presented and compared with the Rayleigh and Tayfun distributions. For all the cases, when the waves propagate in the early stage the exceeding probability increases from the Rayleigh distribution, especially in the tail of the wave crest distribution. Once the waves are fully developed, the tail is on or above the second-order Tayfun distribution.

Furthermore, Fig. 17 illustrates the effect of the crossing angle on the wave crest distribution, but constant directional spreading angle $\Theta = 5^\circ$ and frequency spectral bandwidth $\gamma = 5$ of each component. It is found that the large crests are more likely to be formed at $\Delta\theta = 40^\circ$ and 60° , where the kurtosis is larger. For short-crested crossing systems, the crest distribution is almost independent of the crossing angle, still underestimated by the Tayfun distribution as shown in Fig. 18. The reason for the underestimation is that the second-order Tayfun distribution is based on the narrow-banded hypothesis and does not include the third-order nonlinear effects. In addition, it cannot distinguish between uni- and bimodal seas. The effects of the frequency spectral and directional spreading bandwidth on the wave crest distribution are also investigated. In a narrower frequency spectral or directional spreading wave field, the probability of large crests is higher. Similarly to the probability

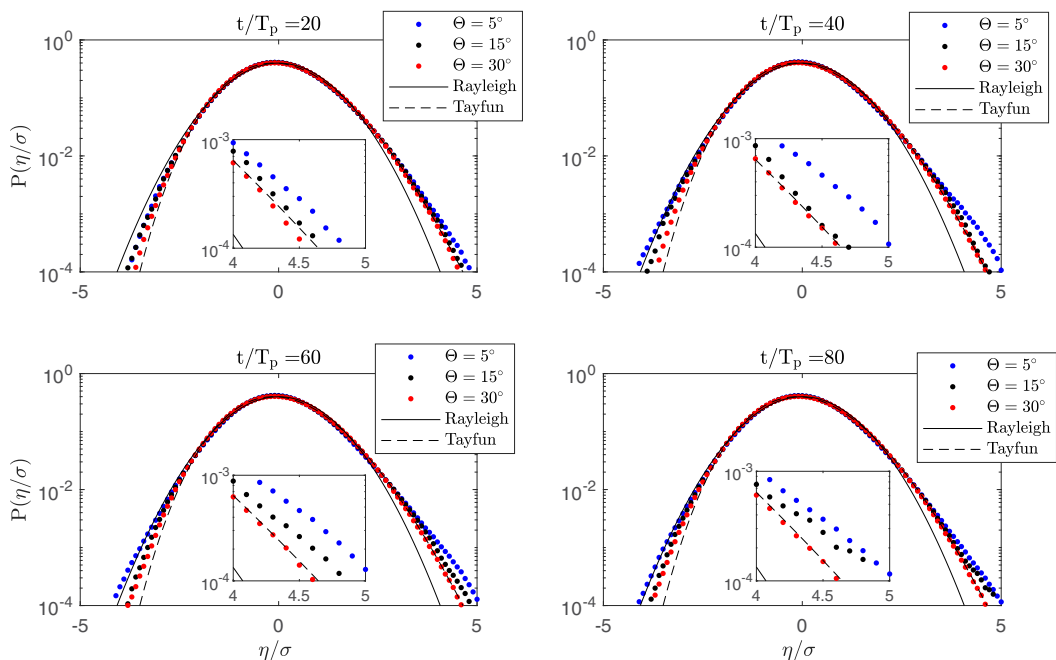


FIG. 16. Probability density function of the surface elevation at different times $t/T_p = 20, 40, 60,$ and 80 . The results show the effect of the directional spreading angle of individual components but constant frequency spectral bandwidth $\gamma = 5$ and crossing angle $\Delta\theta = 40^\circ$. The solid and dashed lines denote the Rayleigh and Tayfun distributions, respectively.

density distribution of surface elevations, the features of the exceedance probability of wave crests generally correlate reasonably well with the kurtosis value.

V. THE OCCURRENCE PROBABILITY OF THE FREAK WAVE

A. Evolution of freak wave occurrence probability

To identify a large freak wave and investigate the evolution of its occurrence probability, we require that the crest height exceeds a certain threshold related to the sea state: $\eta_c > 1.25H_s$.

The freak wave probability P_f is calculated by the exceedance probability for $\eta_c > 1.25H_s$. Figure 19 illustrates the evolution of P_f under varying $\Delta\theta$. The left and right panels are for the nearly long-crested ($\Theta = 5^\circ$) and short-crested ($\Theta = 30^\circ$) cases, respectively. To estimate the convergence of P_f , the error bar is computed by $P_f/\sqrt{N_f}$, where N_f is the number of freak waves. We can observe that P_f increases over a relatively small timescale, owing to the initial strong modulational instability of the wave field. The obtained maximum values are much larger than the second-order prediction obtained by the Tayfun distribution $P_T = 1.28 \times 10^{-4}$. The effect of the crossing angle is significant in the long-crested crossing wave field. For the cases considered here, freak waves are most likely to be formed when $\Delta\theta = 40^\circ$ or $\Delta\theta = 60^\circ$. However, for the broad-spreading cases, the P_f with different $\Delta\theta$ is closely grouped, and the effect of crossing angle is almost negligible.

Figure 20 shows the effect of frequency spectral and directional spreading bandwidth by varying the γ and Θ , respectively. As shown, the P_f generally increases under increasing γ or decreasing Θ .

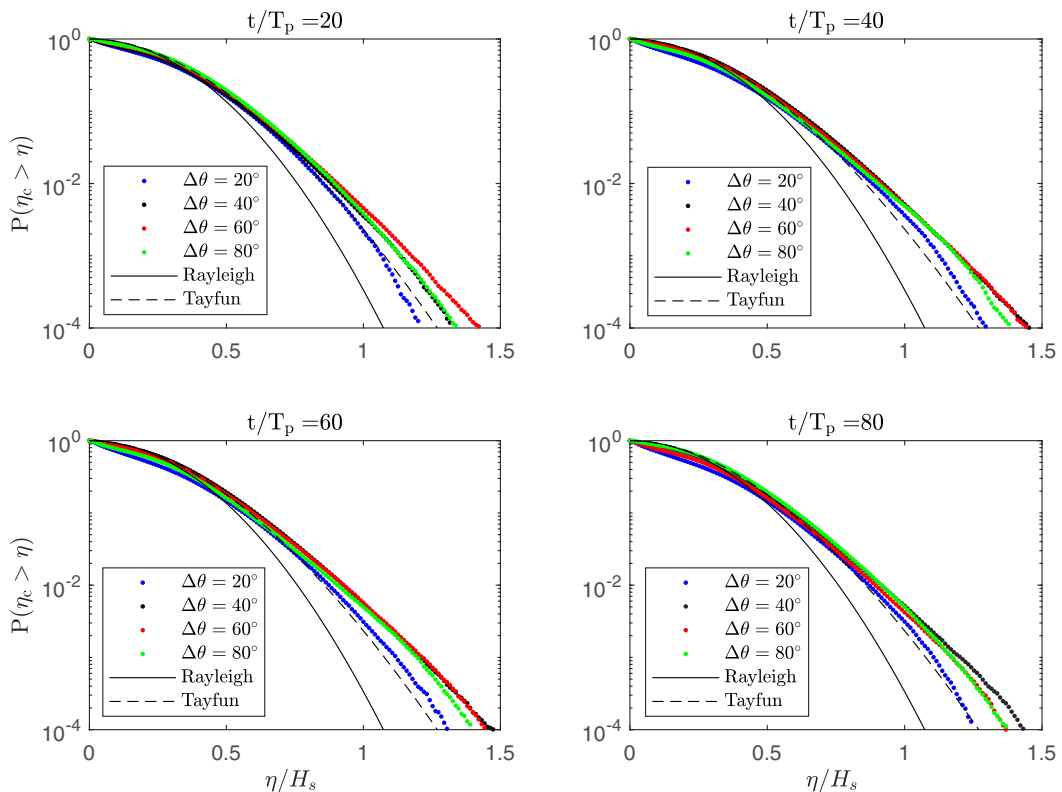


FIG. 17. Exceedance probability of the wave crests at different times $t/T_p = 20, 40, 60,$ and 80 . The results show the effect of changing the crossing angle between different wave systems but under a constant directional spreading $\Theta = 5^\circ$ and frequency bandwidth $\gamma = 5$. The solid and dashed lines denote the Rayleigh and Tayfun distributions, respectively.

B. Dependence of freak wave probability on kurtosis

The probability of freak wave occurrence is considered to depend on the kurtosis of the wave field. A theoretical function called the modified Edgeworth-Rayleigh (MER) distribution [48] is typically used to describe this relation. However, when the directional spreading effect is included, numerical simulations of a large number of wave fields (about 200) by Xiao *et al.* [10] showed that the MER distribution appears to underestimate the occurrence probability. They proposed a new semiempirical formula for the freak wave occurrence probability from the numerical results. However, their simulations only include unimodal sea states. To the best of our knowledge, few studies have validated the correlation between the probability of freak wave occurrence and kurtosis in crossing wave fields, where freak waves are more likely to be formed.

To assess the dependence of the freak wave probability on kurtosis in crossing wave fields, the nondimensional probability of freak wave occurrence P_f/P_T at every output time for each tested case are plotted as a function of the corresponding kurtosis in Fig. 21. We see that P_f/P_T shows a good correlation with the kurtosis. A linear fit holds:

$$P_f/P_T = 10.275 \times (\text{Kur} - 3), \quad (8)$$

where the coefficient of determination is $R^2 = 0.925$.

We also computed the maximum probability of freak wave occurrence P_f^{\max} and maximum kurtosis value Kur^{\max} in each test case. As listed in Table II, the maximum probability P_f^{\max} is

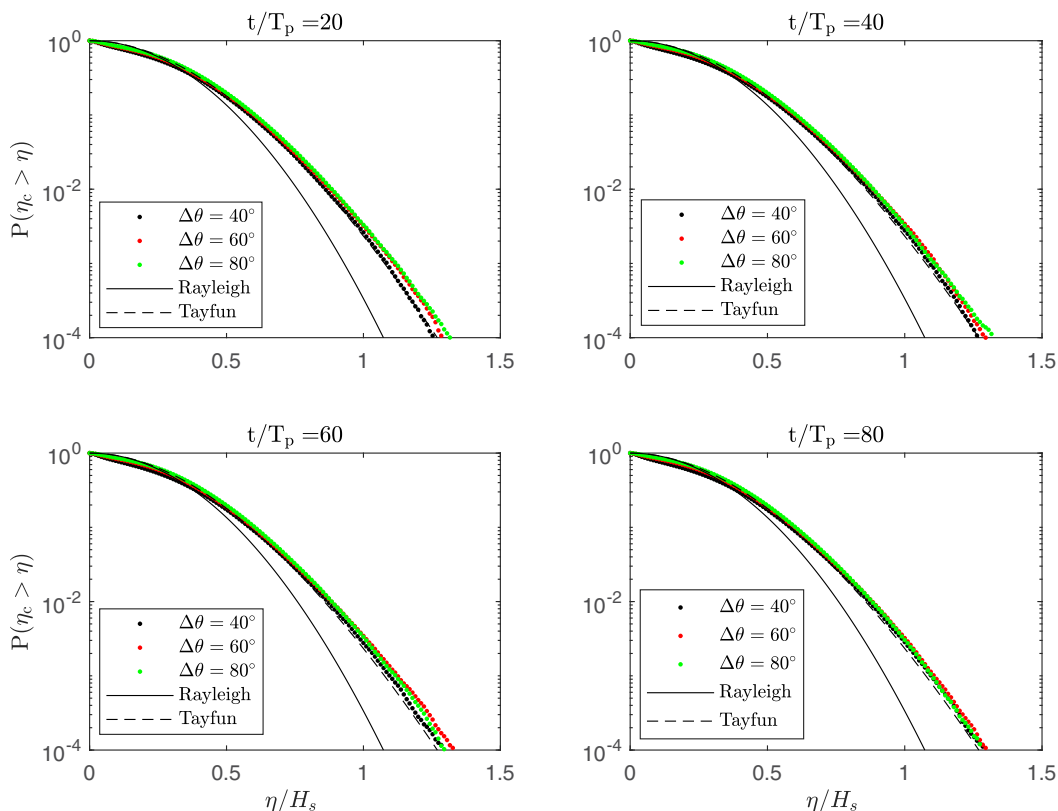


FIG. 18. Exceedance probability of the wave crests at different times $t/T_p = 20, 40, 60,$ and 80 . The results show the effect of changing the crossing angle between different wave systems but constant directional spreading $\Theta = 30^\circ$ and frequency bandwidth $\gamma = 5$. The solid and dashed lines denote the Rayleigh and Tayfun distributions, respectively.

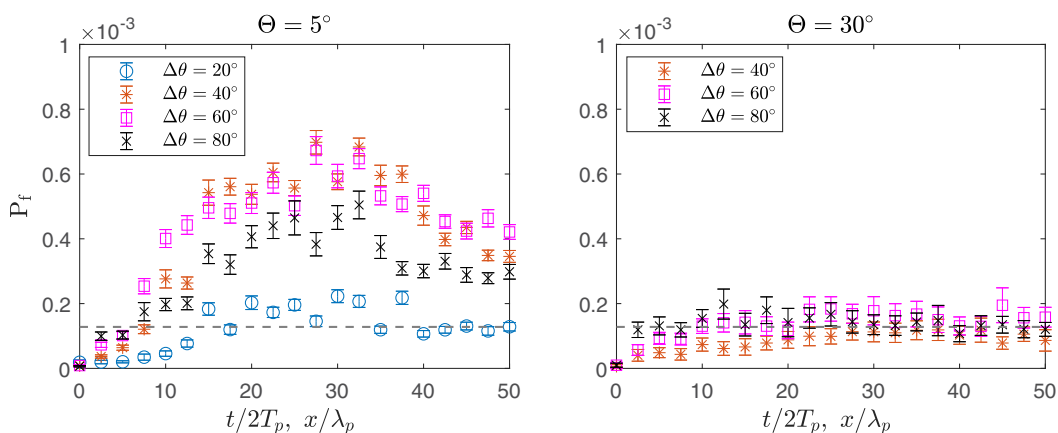


FIG. 19. Evolution of the freak wave probability P_f under varying crossing angle $\Delta\theta$. The left and right panels are for the nearly long-crested ($\Theta = 5^\circ$) and short-crested ($\Theta = 30^\circ$) waves, respectively. The dashed lines represent the second-order prediction obtained by the Tayfun distribution $P_f = 1.28 \times 10^{-4}$.

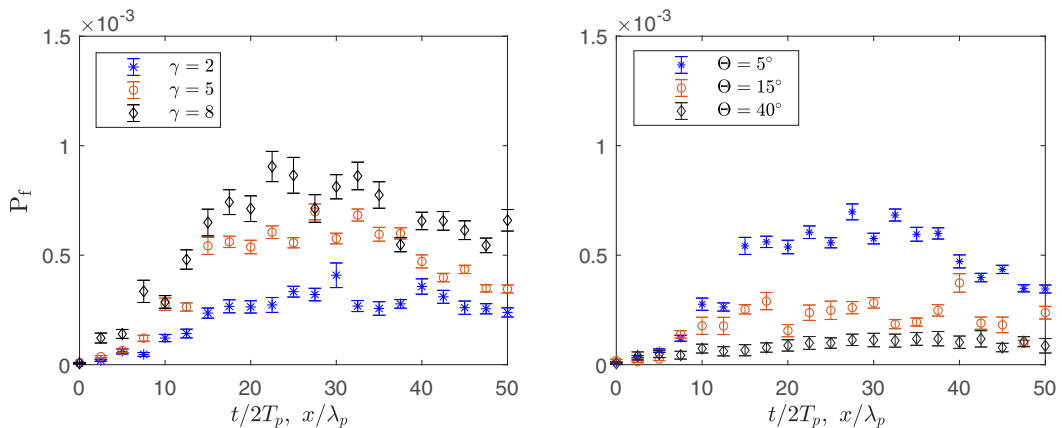


FIG. 20. Effect of the frequency spectrum (left) and directional spreading (right) bandwidth on the evolution of the freak wave occurrence P_f .

larger for larger Kur^{\max} . Therefore, the maximum kurtosis Kur^{\max} is a good indicator of the freak wave occurrence probability.

C. BFI and CBF for prediction of freak wave occurrence

To assess the importance of modulational instability in the wave field, a BFI was proposed by Janssen [6] for a narrow-banded wave field:

$$\text{BFI} = \frac{\sqrt{2}\varepsilon}{\delta_\omega}. \quad (9)$$

Here ε is the wave steepness, and δ_ω is the frequency spectrum bandwidth which can be expressed as:

$$\delta_\omega = \frac{1}{\pi\sqrt{Q_p}}, \quad Q_p = \frac{2\iint f S^2(f, \theta) df d\theta}{(\iint S(f, \theta) df d\theta)^2}, \quad (10)$$

where $S(f, \theta)$ is directional frequency spectrum.

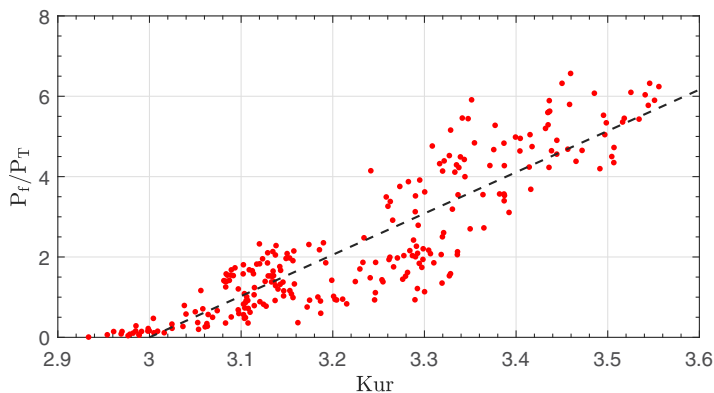


FIG. 21. Dependence of the freak wave occurrence probability on kurtosis. The nondimensional probability of freak wave occurrence P_f/P_T is plotted as a function of the corresponding kurtosis. The dashed line indicates the linear regression result.

TABLE II. The maximum probabilities of freak wave occurrence and the corresponding kurtosis values for all tests.

Test	Kur ^{max}	P_f^{\max}
01	3.2790	2.22×10^{-4}
02	3.4824	6.98×10^{-4}
03	3.4759	6.72×10^{-4}
04	3.3489	5.05×10^{-4}
05	3.1539	1.17×10^{-4}
06	3.1691	1.95×10^{-4}
07	3.1359	1.99×10^{-4}
08	3.3204	4.08×10^{-4}
09	3.6012	9.05×10^{-4}
10	3.2900	3.37×10^{-4}

For waves with significant directional spreading, Mori *et al.* [35] derived a two-dimensional BFI denoted as $\text{BFI}_{2\text{D}}$; it is written as

$$\text{BFI}_{2\text{D}} = \frac{\text{BFI}}{\sqrt{1 + \alpha_2 R_0}}, \quad R_0 = \frac{\delta_\theta^2}{2\delta_\omega^2}, \quad (11)$$

where δ_ω is the directional spreading bandwidth, and α_2 is constant $\alpha_2 = 7.10$ for homogeneous and weakly nonlinear waves. The directional bandwidth δ_θ is calculated via

$$\delta_\theta = \frac{180\sqrt{2}}{\pi} (1 - \sqrt{a^2 + b^2})^{1/2}, \quad (12)$$

with

$$a = \frac{\iint \sin \theta S(f, \theta) df d\theta}{\iint S(f, \theta) df d\theta}, \quad b = \frac{\iint \cos \theta S(f, \theta) df d\theta}{\iint S(f, \theta) df d\theta}. \quad (13)$$

Other attempts to include directional spreading effect have been made in Waseda *et al.* [8] and Xiao *et al.* [10].

In Table III, the indexes BFI and $\text{BFI}_{2\text{D}}$ are computed according to Eqs. (9) and (11), respectively. The spectral quantities δ_ω , δ_θ , BFI, and $\text{BFI}_{2\text{D}}$ are obtained for the crossing wave system and single component, respectively. To distinguish between them, the parameters for the single component are

TABLE III. Values of the spectral parameters of the selected crossing wave tests. The parameters for the single component are marked with an overline.

Test	$\Delta\theta(^{\circ})$	γ	$\Theta(^{\circ})$	$\overline{\delta_\omega}$	$\overline{\delta_\theta}$	$\overline{\text{BFI}}$	$\overline{\text{BFI}_{2\text{D}}}$	δ_ω	δ_θ	BFI	$\text{BFI}_{2\text{D}}$
01	20	5	5	0.14	0.016	0.61	0.59	0.14	0.18	0.86	0.34
02	40	5	5	0.14	0.016	0.61	0.59	0.14	0.35	0.86	0.18
03	60	5	5	0.14	0.016	0.61	0.59	0.14	0.52	0.86	0.12
04	80	5	5	0.14	0.016	0.61	0.59	0.14	0.70	0.86	0.09
05	40	5	30	0.14	0.095	0.61	0.38	0.14	0.36	0.86	0.18
06	60	5	30	0.14	0.095	0.61	0.38	0.14	0.53	0.86	0.12
07	80	5	30	0.14	0.095	0.61	0.38	0.14	0.70	0.86	0.09
08	40	2	5	0.23	0.016	0.38	0.38	0.23	0.35	0.54	0.17
09	40	8	5	0.11	0.016	0.79	0.76	0.11	0.35	1.12	0.19
10	40	5	15	0.14	0.047	0.61	0.51	0.14	0.35	0.86	0.18

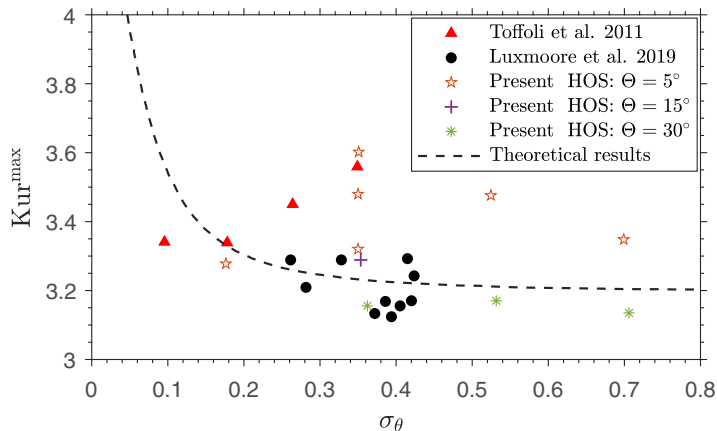


FIG. 22. The maximum observed kurtosis in the total duration versus the directional spreading at the same time/distance.

marked with an overline, i.e., $\overline{\delta_\omega}$, $\overline{\delta_\theta}$, $\overline{\text{BFI}}$, and $\overline{\text{BFI}}_{2\text{D}}$. As shown, as the crossing waves consist of two wave groups with the same peak wave frequency, the δ_ω of total crossing waves is equivalent to that of each component. However, the propagation directions of the two components are different and, correspondingly, δ_θ are much different from $\overline{\delta_\theta}$. Comparing the tests 02, 05, and 10, the δ_θ changes slightly with the variation of the spreading angle Θ . In contrast, as the crossing angle $\Delta\theta$ is varied (i.e., tests 01, 02, 03, and 04), the $\overline{\delta_\theta}$ changes significantly.

A robust correlation between $\text{BFI}/\text{BFI}_{2\text{D}}$ and kurtosis was established for unimodal sea states [35,48] as follows:

$$\text{Kur} = \frac{\pi}{\sqrt{3}}\text{BFI}_{2\text{D}}^2 + 24\varepsilon^2 + 3. \quad (14)$$

Combining Eqs. (9) and (11), it is suggested that the kurtosis depends on the values of ε and δ_ω for unidirectional sea states, and on ε , δ_ω , and δ_θ for directional sea states. Luxmoore *et al.* [30] validated that the kurtosis value in a crossing wave field can be well evaluated from the directional spreading δ_θ using Eq. (14).

We summarize our numerical simulation results and the experimental data [28,30] in Fig. 22, where the maximum observed kurtosis is plotted with respect to the directional spreading. The solid line denotes the theoretical prediction from Eq. (14). For the crossing seas under relatively broad-banded directional spreading $\Theta = 15^\circ$ and 30° , the value of kurtosis can be estimated reasonably well from δ_θ using $\text{BFI}_{2\text{D}}$. However, for the nearly long-crested tests (the experiment in Toffoli *et al.* [28] and our HOS simulations with $\Theta = 5^\circ$), it is seen that the Eq. (14) underestimates the kurtosis. This can be attributed to the fact that $\text{BFI}_{2\text{D}}$ cannot well capture the effect of crossing angle, which is more substantial in nearly long-crested crossing waves. To overcome this, we derived a new form of BFI for crossing seas (named as CBFI) based on the CNLS equations.

To describe the evolution of crossing waves with two identical and symmetrical components, Onorato *et al.* [25] derived the CNLS equations from the Zakharov equation, based on the assumption that both wave systems are narrow banded. Considering the stability analysis of perturbations along the x axis, and using a frame of reference moving with the group velocity (referring to Ref. [25] for more details), the CNLS equations are written as

$$\frac{\partial A}{\partial t} - i\alpha \frac{\partial^2 A}{\partial x^2} + i(\xi|A|^2 + 2\zeta|B|^2)A = 0, \quad (15)$$

$$\frac{\partial B}{\partial t} - i\alpha \frac{\partial^2 B}{\partial x^2} + i(\xi|B|^2 + 2\zeta|A|^2)B = 0, \quad (16)$$

where A and B are the complex amplitudes of the two-wave system, respectively. The corresponding wave numbers are $\mathbf{k}_A = (k, l)$, $\mathbf{k}_B = (k, -l)$, propagating symmetrically along the x axis at an angle $\pm\theta$ ($\theta = \Delta\theta/2$). The coefficients of the CNLS equations are defined as

$$\alpha = \frac{\omega(\kappa)}{8\kappa^4}(2l^2 - k^2), \quad (17)$$

$$\xi = \frac{1}{2}\omega(\kappa)\kappa^2, \quad (18)$$

$$\zeta = \frac{\omega(\kappa)}{2\kappa} \left(\frac{k^5 - k^3l^2 - 3kl^4 - 2k^4\kappa + 2k^2l^2\kappa + 2l^4\kappa}{-2k^2 - 2l^2 + k\kappa} \right), \quad (19)$$

where $\kappa = \sqrt{k^2 + l^2}$ and ω is the corresponding angular frequency. To further analytically investigate the crossing wave system, it is hypothesized that the evolution of two envelopes A and B are identical. Thus, Eqs. (15) and (16) are reduced to

$$\frac{\partial A}{\partial t} + i\frac{1}{8}\frac{\omega(\kappa)}{\kappa^2}\beta\frac{\partial^2 A}{\partial x^2} + i\frac{1}{2}\omega(\kappa)\kappa^2(1 + \gamma)A|A|^2 = 0. \quad (20)$$

The coefficients are written as

$$\beta = \frac{k^2 - 2l^2}{\kappa^2}, \quad (21)$$

$$\gamma = \frac{2k^5 - 2k^3l^2 - 6kl^4 - 4k^4\kappa + 4k^2l^2\kappa + 4l^4\kappa}{(k - 2\kappa)\kappa^4}. \quad (22)$$

Equation (20) allows us to derive a BFI for crossing seas. First, we rewrite the equation in a nondimensional form by introducing the following nondimensional quantities:

$$A' = \frac{A}{\sqrt{2}a}, \quad x' = \Delta kx, \quad t' = \frac{\omega(\kappa)\Delta k^2\beta}{8\kappa^2}t. \quad (23)$$

Here Δk denotes the spectral bandwidth and a corresponds to the wave amplitude. The nondimensional form of Eq. (20) becomes (the primes are omitted for brevity)

$$\frac{\partial A}{\partial t} + i\frac{\partial^2 A}{\partial x^2} + i\left(\frac{2\sqrt{2}\kappa a}{\Delta k/\kappa}\right)^2\frac{\gamma + 1}{\beta}A|A|^2 = 0. \quad (24)$$

A new expression of BFI (denoted as CBFI), is introduced here for crossing waves, according to the ratio of the nonlinear and dispersive terms:

$$\text{CBFI} = \frac{2\sqrt{2}\kappa a}{\Delta k/\kappa} \sqrt{\frac{\gamma + 1}{\beta}}. \quad (25)$$

For more general two-dimensional cases, we obtain

$$\text{CBFI}_{2d} = \text{BFI}_{2d} \sqrt{\frac{\gamma + 1}{\beta}}. \quad (26)$$

The CBFI_{2d} allows us to evaluate the kurtosis (considered an important indicator of freak wave occurrence), using the linear relationship between kurtosis and the squared BFI.

The comparison of the dependence of kurtosis on CBFI_{2d} and BFI_{2d} in crossing seas is shown in Fig. 23. For all data (including the present HOS simulations and previous experiments), when using CBFI_{2d} the scatter in the data is greatly reduced, resulting in a clear and almost linear parametrization of kurtosis and CBFI_{2d}^2 over a wide range of crossing sea states. Based on a linear

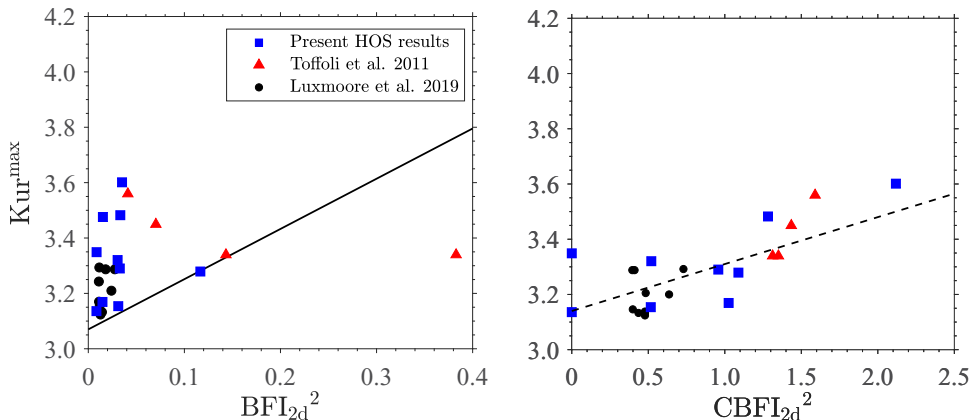


FIG. 23. Dependence of kurtosis on CBFI_{2d} and BFI_{2d} . The black solid line corresponds to the theoretical prediction from Eq. (14). The dashed line represents the linear regression results $\text{Kur} = 0.17 \times \text{CBFI}_{2d}^2 + 3.14$ with a coefficient of determination of $R^2 = 0.67$.

regression analysis, the semiempirical formula is established as

$$\text{Kur} = 0.17 \times \text{CBFI}_{2d}^2 + 3.14, \quad (27)$$

with a coefficient of determination $R^2 = 0.67$. This result shows that CBFI_{2d} is a satisfactory indicator of third-order nonlinearity. To the best of our knowledge, this is the first study to develop a modified BFI for two-component crossing seas in accordance with Onorato *et al.* [27] and validate its relationship with the kurtosis value.

VI. FREAK WAVE SHAPE

The freak wave shape is also an essential parameter in engineering applications. It is well known that the effect of nonlinearity produces high crests and shallow troughs. This feature of vertical asymmetry has been shown in the probability density distribution of surface elevations (see Figs. 13 to 16). Meanwhile, because of the four-wave quaresonant interaction, the wave amplitude becomes horizontal (front-rear) asymmetric along the mean wave direction [36,52].

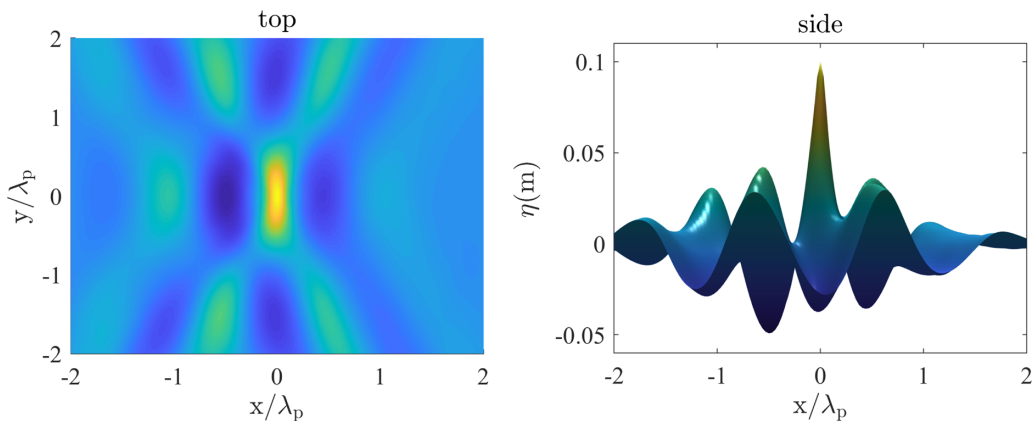


FIG. 24. Examples of average freak wave shape: top (left) and side (right) views. Conditions: $\Delta\theta = 20^\circ$, $\gamma = 5$, and $\Theta = 5^\circ$.

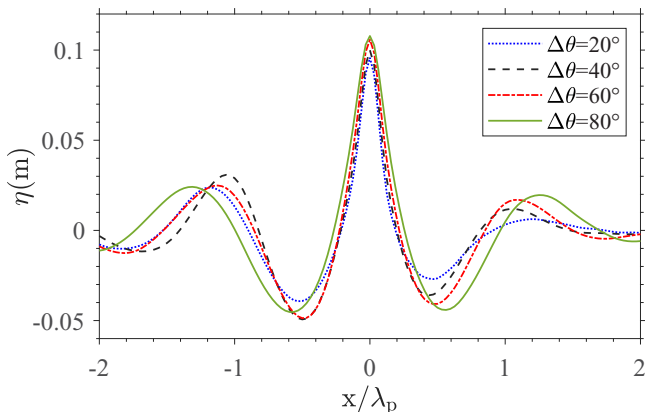


FIG. 25. Effect of varying crossing angle on average wave shape under a constant frequency width $\gamma = 5$ and directional spreading $\Theta = 5^\circ$.

The average freak wave shape is defined as [36]

$$\bar{\eta}(x, y) = \langle \eta'_{\text{freak}}(x, y) \rangle, \quad (28)$$

where $\eta'_{\text{freak}}(x, y)$ is the surface elevation after shifting the freak wave crests to $x = 0$ and $y = 0$. A typical example is shown in Fig. 24. In the left panel of Fig. 24, contour maps of the surface elevation are shown; in the right panel, the side view of the averaged freak wave is taken along the mean propagation direction. Vertical and horizontal asymmetries are observed: The front trough (to the right of the crest) is shallower than the rear trough (left of the crest) and its modulus is much smaller than the crest amplitude.

To compare the freak wave shapes in different cases, we analyzed the wave profile in the mean wave direction, as shown in Fig. 25; this indicates the effect of the crossing angle with a constant frequency spectral and directional spreading bandwidth in long-crested seas. For the smallest crossing angle seas ($\Delta\theta = 20^\circ$), the rear trough is deeper than the front trough. With the increasing crossing angle, the difference between the front and rear trough is significantly reduced. The wave shape in the case of the largest crossing angle ($\Delta\theta = 80^\circ$) seems symmetric: The depth of the rear trough nearly matches that of the front trough. For the feature of vertical asymmetry related to the effect of second-order nonlinearity, the freak wave with the higher crest and deeper trough

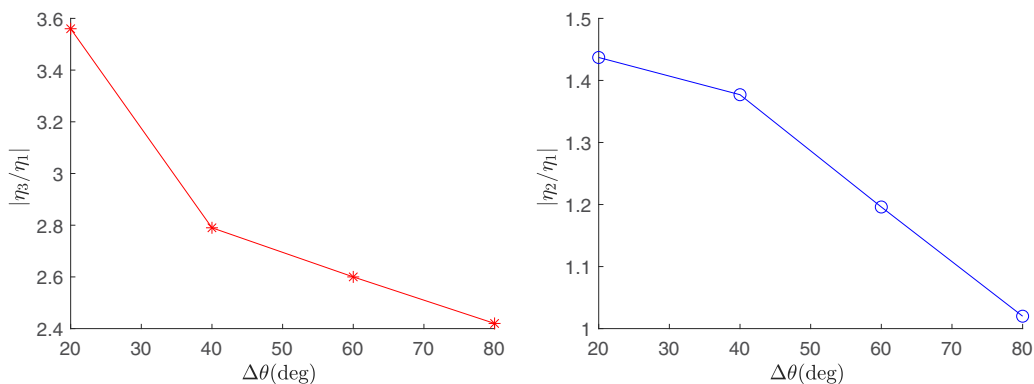


FIG. 26. The horizontal (left) and vertical (right) asymmetry indices as a function of the crossing angle for constant directional spreading $\Theta = 5^\circ$ and frequency width $\gamma = 5$.

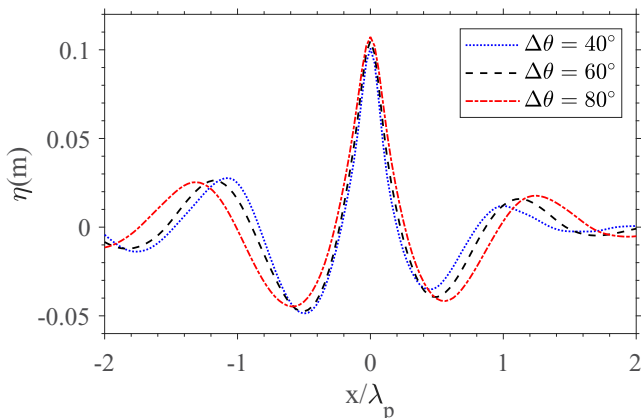


FIG. 27. Effect of crossing angle on average wave shape under a constant frequency width $\gamma = 5$ and a constant directional spreading $\Theta = 30^\circ$.

is observed in the sea condition of larger crossing angle. From this observation, it is conjectured that the effect of second-order nonlinearity is suppressed when the crossing angle increases. This is consistent with the results for skewness (see Fig. 8).

To investigate the freak wave shape more quantitatively, following Dysthe *et al.* [53], the vertical asymmetry is measured using the ratio between the crest height η_3 and the nearest trough depth (i.e., the rear trough depth η_1). The asymmetry of the wave amplitude in the mean wave direction is defined as the ratio between the depth of the front trough η_2 and that of the rear trough η_1 . These two asymmetry indexes are plotted as a function of the crossing angle in Fig. 26. It is more apparent that the vertical and horizontal asymmetries are reduced with the increasing crossing angle. For the largest-angle case ($\Delta\theta = 80^\circ$), the vertical asymmetry index is $|\eta_3/\eta_1| = 2.4$ and the wave is nearly symmetrical in the mean horizontal direction with $|\eta_2/\eta_1| = 1.0$. Here, the value of the vertical asymmetry index $|\eta_3/\eta_1|$ exceeds that of the unimodal sea, which is typically ~ 2.3 [51,54]. This result suggests that the four-wave quasiresonant interaction is enhanced by the nonlinear interactions between the two wave systems. As discussed in Fujimoto *et al.* [36], a front-rear symmetrical freak wave shape is observed in the JKEO-Broad case. They explained this finding from the perspective of the directional spectrum bandwidth. Our results provide another way of understanding the symmetrical freak wave shape in the JKEO-Broad case: the large crossing angle

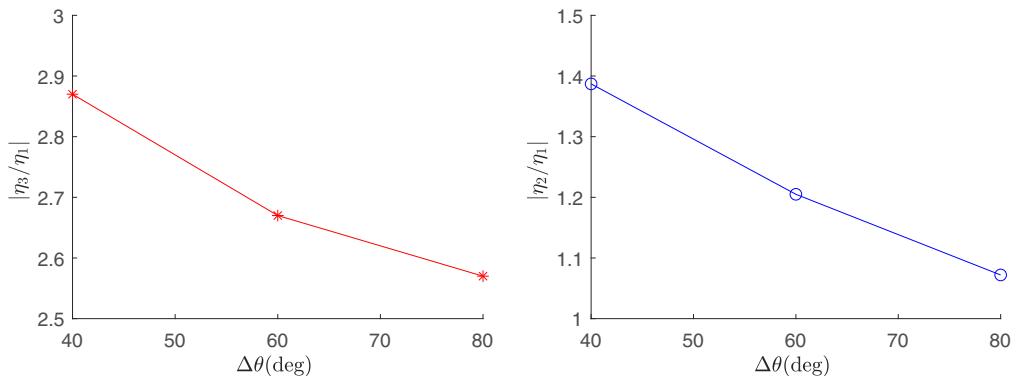


FIG. 28. Effect of crossing angle on average wave shape under a constant directional spreading $\Theta = 30^\circ$ and a constant peak enhancement factor $\gamma = 5$.

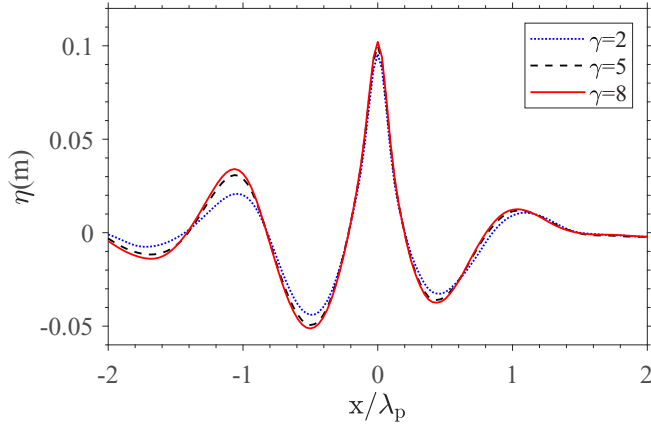


FIG. 29. The wave shape in the mean propagation direction for a varying peak enhancement factor γ but a constant crossing angle $\Delta\theta = 40^\circ$ and a constant directional spreading $\Theta = 5^\circ$.

between the two wave systems. For short-crested crossing systems (as shown in Figs. 27 and 28), increasing the crossing angle reduces the vertical and horizontal asymmetries.

Figure 29 shows the averaged wave shape for the varying frequency peak enhancement factor γ . As γ increases, the frequency spectrum becomes narrow, and the nonlinear effect intensifies, resulting in a slight increase in the crest height. However, the trough depth is reduced, which is consistent with the probability density distribution of the troughs (see Fig. 15). Quantitatively, the asymmetry indexes are $|\eta_3/\eta_1| = 2.93, 2.80, 2.72$ and $|\eta_2/\eta_1| = 1.36, 1.38, 1.36$ for $\gamma = 2, 5, 8$, respectively.

Figure 30 illustrates the effect of directional spreading on the wave shape. Interestingly, no significant difference was observed in behavior as a function of the directional spreading angle Θ . The asymmetry indexes are approximately $|\eta_3/\eta_1| = 2.73$ and $|\eta_2/\eta_1| = 1.30$, respectively.

A comparison of the wave profiles in Figs. 25, 29, and 30 clearly shows that the crossing angle between the two components rather than the frequency or directional spectrum bandwidth of each wave component has a greater effect on the freak wave shape.

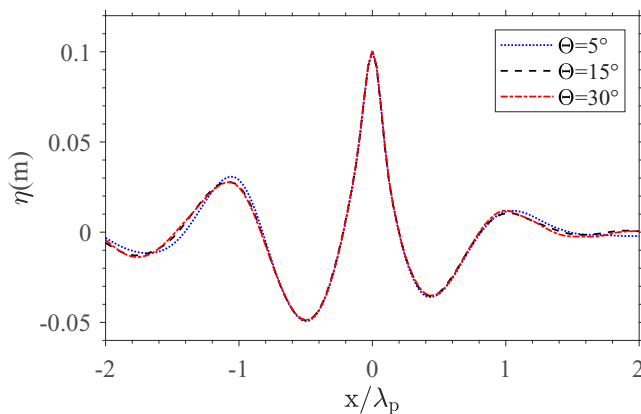


FIG. 30. The wave shape in the mean propagation direction for a varying directional spreading Θ but a constant crossing angle $\Delta\theta = 40^\circ$ and a constant peak enhancement factor $\gamma = 5$.

VII. CONCLUDING REMARKS

We studied the nonlinear wave statistics and freak waves in crossing seas. Direct numerical simulations of several typical crossing seas were performed using the HOS method. The dynamical statistics of surface waves are fully characterized, including the wave spectra, exceedance probability of wave crests, probability density distribution of surface elevation, the kurtosis and skewness, freak wave occurrence probability, and the freak wave shape which has received less attention in previous studies. The accuracy and reliability of the present numerical model in describing the wave statistics are demonstrated by extensive comparisons with the experiments [28,30,47].

The effects of the crossing angle between the two components, directional spreading, and frequency spectrum of individual systems on nonlinear statistics are investigated. For the crossing seas consisting of two long-crested waves, our numerical results confirmed that the kurtosis increases when the angle is close to 40° or 60° . As a result, the lower and upper tails of the probability density distribution of the surface elevation, and the tail of the exceedance probability of wave crest amplitude are significantly higher than the second-order results. For the crossing seas consisting of two short-crested waves, the kurtosis is closely grouped and independent of the angle. The surface elevation and crest distribution are generally in agreement with the second-order results. In addition, the kurtosis increases for a narrower directional spreading or frequency spectrum, and the tails of the surface elevation and crest distribution are enhanced.

To assess the effect of third-order nonlinearity and thereby predict the probability of freak wave occurrence, we confirmed that the kurtosis can be generally estimated by the overall mean directional spreading for crossing directional seas, which is first applied by Luxmoore *et al.* [30]. However, when both of the two components are long-crested, the kurtosis tends to be underestimated. To overcome this, a Coupled BFI (CBFI) is derived for crossing seas to capture the effect of third-order nonlinearity in accordance with Onorato *et al.* [27]. Our numerical results show that the kurtosis can be estimated reasonably well from CBFI over a broad range of frequency bandwidths and directional spreading values.

The freak wave shape is more affected by the crossing angle between the two wave components than the frequency or directional spectrum bandwidth of each component. Under an increase in the crossing angle, both the vertical and horizontal asymmetries are reduced.

ACKNOWLEDGMENTS

The financial support from the National Natural Science Foundation of China with Grant No. 52171269 is gratefully acknowledged. X.Z., S.L., and J.Y. are very grateful to the financial support by the Oceanic Interdisciplinary Program of Shanghai Jiao Tong University (Project No. SL2021PT205).

APPENDIX: CONVERGENCE TEST

A large number of datasets are required to minimize the level of statistical uncertainty in the surface-wave statistical properties. Convergence tests of the present numerical simulations have been performed for the kurtosis, skewness, and wave shape factor. Figure 31 shows the 95% confidence intervals and the ensemble value of the achieved maximum kurtosis as a function of the number of realizations for the three typical sea states. The result for skewness is presented in Fig. 32. We verified that 30 realizations can produce stable estimates of the statistical moments. The 95% confidence intervals are smaller than ± 0.08 for the kurtosis and ± 0.02 for the skewness.

To test the influence of the ramping period t_a , the evolutions of the crossing seas with different t_a are simulated and compared. The results of kurtosis are shown in Fig. 33. It is found that, the value of t_a only affects the evolution of the kurtosis during the initial stage. The maximum values in which we are most interested are very close. This is because the second-order and third-order harmonics are well captured in all the cases. In addition, referring to Dommermuth [46], the amplitude oscillations of second-order and third-order harmonics are nonsignificant, even when $t_a = 2T_p$.

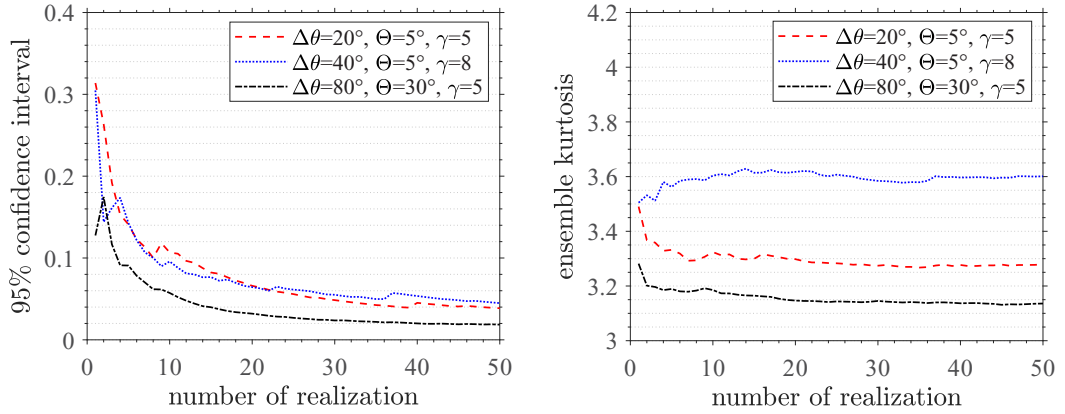


FIG. 31. Convergence tests of the maximum kurtosis as a function of the number of realizations. The left and right panels show the 95% confidence intervals and the ensemble value, respectively.

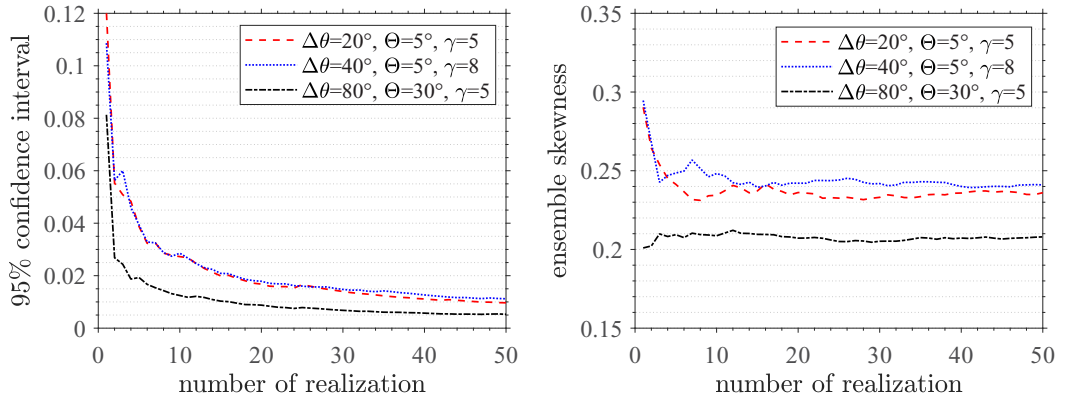


FIG. 32. Convergence tests of the maximum skewness as a function of the number of realizations. The left and right panels show the 95% confidence intervals and the ensemble value, respectively.

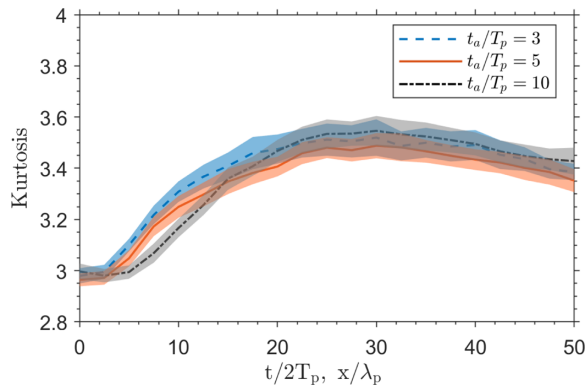


FIG. 33. The effect of the ramping period t_a on the evolution of the kurtosis.

- [1] J. R. Halliday and D. G. Dorrell, Review of wave energy resource and wave generator developments in the UK and the rest of the world, in *Proceedings of the 4th IASTED International Conference on Power and Energy Systems* (IASTEN, Calgary, 2004), Vol. 442, p. 136.
- [2] B. S. White and B. Fornberg, On the chance of freak waves at sea, *J. Fluid Mech.* **355**, 113 (1998).
- [3] J. L. Bona and J. C. Saut, Dispersive blowup of solutions of generalized Korteweg-de Vries equations, *J. Differ. Equ.* **103**, 3 (1993).
- [4] E. Pelinovsky, T. Talipova, A. Kurkin, and C. Kharif, Nonlinear mechanism of tsunami wave generation by atmospheric disturbances, *Nat. Hazards Earth Syst. Sci.* **1**, 243 (2001).
- [5] V. E. Zakharov and L. A. Ostrovsky, Modulation instability: The beginning, *Physica D* **238**, 540 (2009).
- [6] P. A. E. M. Janssen, Nonlinear four wave interactions and freak waves, *J. Phys. Oceanogr.* **33**, 863 (2003).
- [7] M. Onorato, L. Cavaleri, S. Fouques, O. Gramstad, P. Janssen, J. Monbaliu, A. R. Osborne, C. Pakozdi, M. Serio, and C. T. Stansberg, Statistical properties of mechanically generated surface gravity waves: A laboratory experiment in a three-dimensional wave basin, *J. Fluid Mech.* **627**, 235 (2009).
- [8] T. Waseda, T. Kinoshita, and H. Tamura, Evolution of a random directional wave and freak wave occurrence, *J. Phys. Oceanogr.* **39**, 621 (2009).
- [9] A. Toffoli, O. Gramstad, K. Trulsen, J. Monbaliu, E. Bitner-gregersen, and M. Onorato, Evolution of weakly nonlinear random directional waves: Laboratory experiments and numerical simulations, *J. Fluid Mech.* **664**, 313 (2010).
- [10] W. Xiao, Y. Liu, G. Wu, and D. K. P. Yue, Rogue wave occurrence and dynamics by direct simulations of nonlinear wave-field evolution, *J. Fluid Mech.* **720**, 357 (2013).
- [11] P. A. E. M. Janssen and M. Onorato, The intermediate water depth limit of the Zakharov equation and consequences for wave prediction, *J. Phys. Oceanogr.* **37**, 2389 (2007).
- [12] A. Toffoli, L. Fernandez, J. Monbaliu, M. Benoit, E. Gagnaire-Renou, J. M. Lefèvre, L. Cavaleri, D. Proment, C. Pakozdi, C. T. Stansberg, T. Waseda, and M. Onorato, Experimental evidence of the modulation of a plane wave to oblique perturbations and generation of rogue waves in finite water depth, *Phys. Fluids* **25**, 091701 (2013).
- [13] F. Fedele, J. Brennan, S. Ponce de León, J. Dudley, and F. Dias, Real world ocean rogue waves explained without the modulational instability, *Sci. Rep.* **6**, 27715 (2016).
- [14] C. G. Soares and T. Moan, Model uncertainty in the long-term distribution of wave-induced bending moments for fatigue design of ship structures, *Mar. Struct.* **4**, 295 (1991).
- [15] T. A. A. Adcock, P. H. Taylor, S. Yan, Q. W. Ma, and P. A. E. M. Janssen, Did the Draupner wave occur in a crossing sea? *Proc. Math. Phys. Eng. Sci.* **467**, 3004 (2011).
- [16] M. L. Mcallister, S. Draycott, T. Adcock, P. H. Taylor, and T. S. Van den Bremer, Laboratory recreation of the Draupner wave and the role of breaking in crossing seas, *J. Fluid Mech.* **860**, 767 (2019).
- [17] U. F. de Pinho, P. C. Liu, and C. E. P. Ribeiro, Freak waves at Campos Basin, Brazil, *Geofizika* **21**, 53 (2004).
- [18] W. Rosenthal and S. Lehner, Rogue Waves: Results of the MaxWave Project, *J. Offshore Mech. Arct. Eng.* **130**, 021006 (2008).
- [19] A. Toffoli, J. M. Lefèvre, E. Bitner-Gregersen, and J. Monbaliu, Towards the identification of warning criteria: Analysis of a ship accident database, *Appl. Ocean Res.* **27**, 281 (2005).
- [20] Z. Zhang and X. Li, Global ship accidents and ocean swell-related sea states, *Nat. Hazards Earth Syst. Sci.* **17**, 2041 (2017).
- [21] H. Tamura, T. Waseda, and Y. Miyazawa, Freakish sea state and swell-windsea coupling: Numerical study of the Suwa-Marui incident, *Geophys. Res. Lett.* **36**, 329 (2009).
- [22] L. A. Cavaleri, L. A. Bertotti, L. B. Torrisi, E. C. Bitner-Gregersen, and M. D. Onorato, Rogue waves in crossing seas: The Louis Majesty accident, *J. Geophys. Res. Oceans* **117**, C00J10 (2012).
- [23] K. Trulsen, J. C. N. Borge, O. Gramstad, L. Aouf, and J. M. Lefèvre, Crossing sea state and rogue wave probability during the Prestige accident, *J. Geophys. Res. Oceans* **120**, 7113 (2015).
- [24] F. Fedele, C. Lugni, and A. Chawla, The sinking of the El Faro: predicting real world rogue waves during Hurricane Joaquin, *Sci. Rep.* **7**, 11188 (2017).
- [25] M. Onorato, A. R. Osborne, and M. Serio, Modulational Instability in Crossing Sea States: A Possible Mechanism for the Formation of Freak Waves, *Phys. Rev. Lett.* **96**, 014503 (2006).

- [26] P. K. Shukla, I. Kourakis, B. Eliasson, M. Marklund, and L. Stenflo, Instability and Evolution of Nonlinearly Interacting Water Waves, *Phys. Rev. Lett.* **97**, 094501 (2006).
- [27] M. Onorato, D. Proment, and A. Toffoli, Freak waves in crossing seas, *Eur. Phys. J. Spec. Top.* **185**, 45 (2010).
- [28] A. Toffoli, E. M. B. Bitner-Gregersen, A. R. Osborne, M. Serio, and M. Onorato, Extreme waves in random crossing seas: Laboratory experiments and numerical simulations, *Geophys. Res. Lett.* **38**, 122 (2011).
- [29] E. M. Bitner-Gregersen and A. Toffoli, Occurrence of rogue sea states and consequences for marine structures, *Ocean Dyn.* **64**, 1457 (2014).
- [30] J. Luxmoore, S. Ilic, and N. Mori, On kurtosis and extreme waves in crossing directional seas: A laboratory experiment, *J. Fluid Mech.* **876**, 792 (2019).
- [31] O. Gramstad and K. Trulsen, Fourth-order coupled nonlinear Schrödinger equations for gravity waves on deep water, *Phys. Fluids* **23**, 062102 (2011).
- [32] K. Trulsen and K. B. Dysthe, A modified nonlinear Schrödinger equation for broader bandwidth gravity waves on deep water, *Wave Motion* **24**, 281 (1996).
- [33] O. Gramstad, E. M. Bitner-Gregersen, K. Trulsen, and J. Nieto-Borge, Modulational instability and rogue waves in crossing sea states, *J. Phys. Oceanogr.* **48**, 1317 (2018).
- [34] J. Brennan, J. Dudley, and F. Dias, Extreme waves in crossing sea states, *Int. J. Ocean Coast. Eng.* **1**, 1850001 (2018).
- [35] N. Mori, M. Onorato, and P. A. E. M. Janssen, On the estimation of the kurtosis in directional sea states for freak wave forecasting, *J. Phys. Oceanogr.* **41**, 1484 (2011).
- [36] W. Fujimoto, T. Waseda, and A. Webb, Impact of the four-wave quasi-resonance on freak wave shapes in the ocean, *Ocean Dyn.* **69**, 101 (2019).
- [37] J. J. Xie, Y. Ma, G. Dong, and M. Perlin, Numerical investigation of third-order resonant interactions between two gravity wave trains in deep water, *Phys. Rev. Fluids* **6**, 014801 (2021).
- [38] D. G. Dommermuth and D. K. P. Yue, A high-order spectral method for the study of nonlinear gravity waves, *J. Fluid Mech.* **184**, 267 (1987).
- [39] B. J. West, K. A. Brueckner, R. S. Jand, D. Milder, and R. Milton, A new method for surface hydrodynamics, *J. Geophys. Res.* **92**, 11803 (1987).
- [40] V. Zakharov, Stability of period waves of finite amplitude on surface of a deep fluid, *J. Appl. Mech. Tech. Phys.* **9**, 190 (1968).
- [41] S. Stole-Hentschel, K. Trulsen, B. Lisa, and R. Anne, Extreme wave statistics of counter-propagating, irregular, long-crested sea states, *Phys. Fluids* **30**, 067102 (2018).
- [42] S. Liu and X. Zhang, Extreme wave crest distribution by direct numerical simulations of long-crested nonlinear wave fields, *Appl. Ocean Res.* **86**, 141 (2019).
- [43] T. Kokina and F. Dias, Influence of computed wave spectra on statistical wave properties, *J. Mar. Sci. Eng.* **8**, 1023 (2020).
- [44] M. Tanaka, Verification of Hasselmann's energy transfer among surface gravity waves by direct numerical simulations of primitive equations, *J. Fluid Mech.* **444**, 199 (2001).
- [45] M. Tanaka and N. Yokoyama, Effects of discretization of the spectrum in water-wave turbulence, *Fluid Dyn. Res.* **34**, 199 (2004).
- [46] D. G. Dommermuth, The initialization of nonlinear waves using an adjustment scheme, *Wave Motion* **32**, 307 (2000).
- [47] A. D. Sabatino and M. Serio, Experimental investigation on statistical properties of wave heights and crests in crossing sea conditions, *Ocean Dyn.* **65**, 707 (2015).
- [48] N. Mori and P. A. E. M. Janssen, On kurtosis and occurrence probability of freak waves, *J. Phys. Oceanogr.* **36**, 1471 (2006).
- [49] F. Fedele, On the kurtosis of deep-water gravity waves, *J. Fluid Mech.* **782**, 25 (2015).
- [50] M. A. Tayfun, Narrow-band nonlinear sea waves, *J. Geophys. Res. Oceans* **85**, 1548 (1980).
- [51] H. Socquet-juglard, K. Dysthe, K. Trulsen, H. E. Krogstad, and J. Liu, Probability distributions of surface gravity waves during spectral changes, *J. Fluid Mech.* **542**, 195 (2005).

- [52] T. A. A. Adcock and P. H. Taylor, Fast and local non-linear evolution of steep wave-groups on deep water: A comparison of approximate models to fully non-linear simulations, [Phys. Fluids](#) **28**, 016601 (2016).
- [53] K. Dysthe, H. E. Krogstad, and P. Müller, Oceanic rogue waves, [Annu. Rev. Fluid Mech.](#) **40**, 287 (2008).
- [54] C. G. Soares, Z. Cherneva, and E. M. Antao, Characteristics of abnormal waves in north sea storm sea states, [Appl. Ocean Res.](#) **25**, 337 (2003).